Strain Partitioning Between Ductile and Brittle Stratigraphy—Characterizing the Sand Wash Fault System, Uinta Basin, Utah

Riley Brinkerhoff[1], John McBride[2], Sam Hudson[2], Douglas A. Sprinkel[3], Ron Harris[2], Kevin Rey[2], and Eric Tingey[2]

[1]*Wasatch Energy Management, LLC, Provo, Utah, rbrinkerhoff@wemenergy.com*

[2]*Department of Geological Sciences, BYU, Provo, Utah*

[3]*Aztec GeoSolutions, Pleasant View, Utah*

ABSTRACT

The Sand Wash fault zone is a segmented and discontinuous fault system that strikes northwest to southeast in the central part of the Uinta Basin. It is approximately 34 kilometers long with an uncommonly wide damage zone, typically 100 to 200 meters wide. Due to recent, rapid, and large-scale incision by the Green River and its tributaries, the Sand-Wash fault zone is well exposed in several closely spaced canyons. These canyon exposures allow mapping of the lateral relationships through panoramic photographs and surface kinematic descriptions.

Most movement on the Sand Wash fault zone occurred in the late Eocene, but minor, more recent movement likely occurred. Evidence for fault timing includes strata-bound, syndepositional movement which occurred during Lake Uinta time (55 to 43 Ma BP) resulting in debris flows, slump blocks, and small (>150 meters diameter) sag basins filled with poorly organized sediments. After lithification, elongate grabens formed with up to 33.5 meters of horizontal extension. Two styles of deformation are present. Brittle rocks, such as sandstone and limestone beds, are intensely fractured and faulted, whereas clay and organic-rich rocks are largely unfractured and unfaulted, with variably folded beds that have experienced some layer-parallel slip. Laterally, deformation is distributed up to 100 meters from the fault core, which is uncommonly large for faults with short lengths and little displacement. Vertically, displacement is concentrated in brittle sandstone and carbonate beds and rare in clay- and hydrocarbon-rich units, such as the Mahogany oil-shale zone of the Eocene Green River Formation. The Mahogany oil-shale zone mostly displays ductile flow (granular flow) commonly forming small décollements between overlying and underlying units. Vertical displacement on separate fault segments is generally less than 5 meters and decreases down section, dying out completely around the top of the Mahogany oil-shale zone.

In this paper we show evidence for syndepositional deformation along the Sand Wash fault zone, strain partitioning along décollement surfaces, fault surfaces that experience multiple deformational phases, pop-up blocks, and graben development. We also show that deformation on the fault zone is related to extension above a neutral surface of a larger fold. This larger fold is associated with a basement-rooted fault zone that moved during Laramide tectonism as the Uncompahgre uplift developed. The Sand Wash fault zone appears to have many similarities to the larger, and more deeply buried, Duchesne fault zone 25 kilometers to the north, and the more deeply eroded Cedar Ridge fault zone located 30 kilometers to the south. The high-resolution fault model, developed herein, is thus a good proxy for other complex fault zones in the Uinta Basin. Our model will be useful to oil and gas operators as they develop horizontal wells across this and other complex fault zones in the basin.

INTRODUCTION AND PREVIOUS WORK

Utah is justifiably famous for its outstanding outcrops, with stratigraphers coming from all over the world to study the well-exposed Upper Cretaceous deltaic and marine outcrops in the Book Cliffs, and lacustrine beds of the Eocene Green River Formation (GRF) in the Uinta Basin. Likewise, structural geologists come to see well-exposed examples of thin-skinned thrust faults of the Sevier orogeny, basement-rooted reverse faults of the Laramide orogeny, salt withdrawal faulting in the Paradox Basin, and active fault systems related to the extension of the Basin and Range province. The superbly exposed Moab Fault alone attracts hundreds of geology students and professionals every year. To the above list we add the Sand Wash fault zone (SWFZ) in the central Uinta Basin, one of the most complex, and clearly exposed examples of geologic deformation in Utah (figure 1).

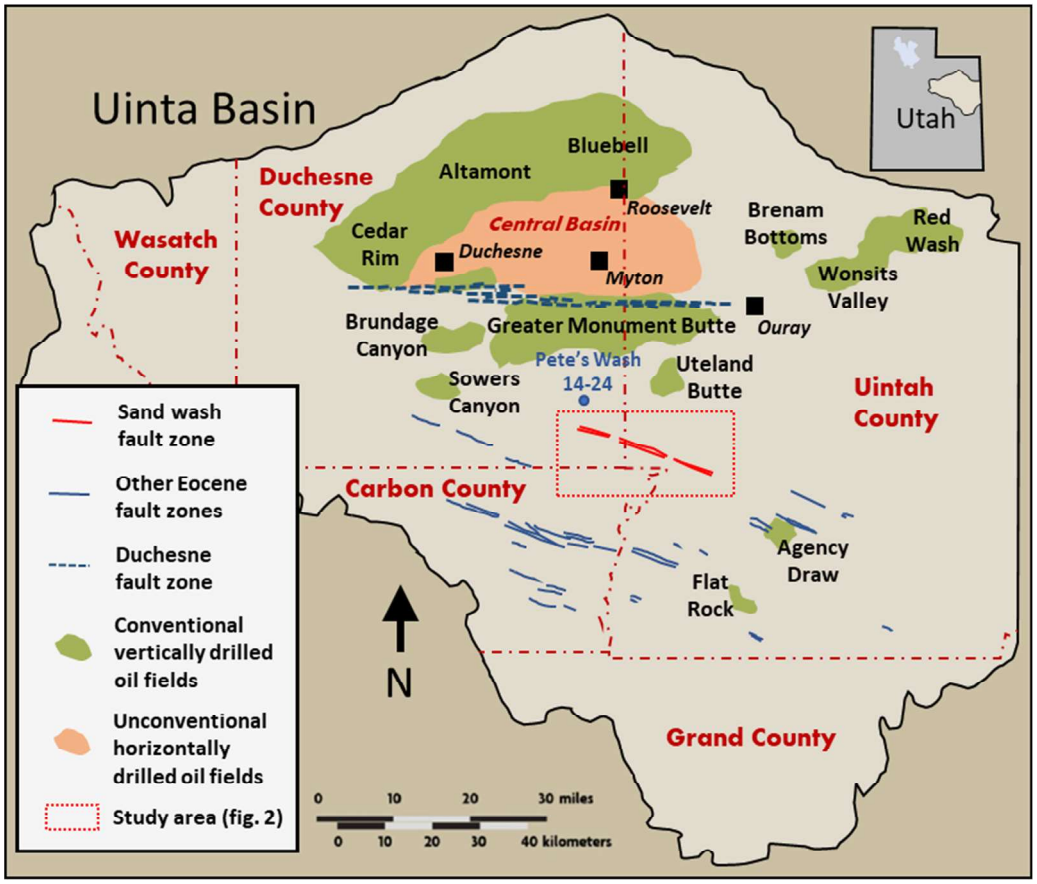

Figure 1. *Location map of the Uinta Basin within northeastern Utah, showing the position of the Sand Wash fault zone (SWFZ) in red in the center of the basin. Note that the SWFZ is south of the main oil and gas fields in the basin and that it trends northwest-southeast, like the other fault zones in the southern Uinta Basin.*

Fault mechanics are commonly oversimplified. A common mistake is to assume that the same magnitude of offset observed in a single outcrop is uniform along the entire fault. In most cases, however, faults rapidly change character in response to varying mechanical properties of the rocks involved in the deformation. Other factors, such as pore fluid pressure change between rock units, can also cause a lack of uniformity. The SWFZ is a unique natural laboratory for the study of variable fault mechanics.

The SWFZ gets its name from exposures in Sand Wash, a deeply incised canyon that drains into the Green River, near the head of Desolation Canyon, in northeastern Utah. The SWFZ is a segmented and discontinuous fault system that can be divided into eastern and western parts by the course of the Green River (figure 2). Highly deformed sedimentary strata is commonly sandwiched by strata that is largely undeformed at the outcrop scale, resulting in vertically partitioned units (figure 3).

Our study focuses on outcrop located where the lower reaches of Sand Wash and Nine Mile Creek drain into the Green River (figure 4). There, the SWFZ includes examples of syndepositional soft-sediment deformation, small décollements, reactivated fault surfaces, and alternating ductile and brittle deformational relationships within the Green River Formation. These structural features are beautifully exposed in three dimensions (3D) due to erosion in Sand Wash and its tributary canyons, having exposed 800 meters of section across and along the length of the fault zone.

For such a well exposed fault system, very little has been published about it. The SWFZ is exceptionally long and straight for the little observed slip on its many faults. The high degree of deformation in some sandstone beds adjacent to apparently undeformed oil -shale beds creates very visually striking outcrops. Many parallel fault systems in the central and southern Uinta Basin have been interpreted by previous workers as having significant strike-slip offset (Stone, 1977; Eckels and others, 2004; Bader, 2009; Sprinkel, 2018; Brinkerhoff and Sprinkel, 2021). Here we examine the SWFZ for transpressional features as well. As perhaps the best exposed fault system in the Uinta Basin, the SWFZ offers an outstanding opportunity to understand the Laramide stresses that created it. The data collected in many field visits suggests a simple extensional model that points to significant deeper deformation.

GEOLOGIC SETTING AND BACKGROUD INFORMATION

The Uinta Basin formed as a rapidly subsiding flexural basin during the Laramide orogeny by loading of the adjacent Uinta Mountains uplift to the north (figure 5). Paleogene sedimentary units accumulated

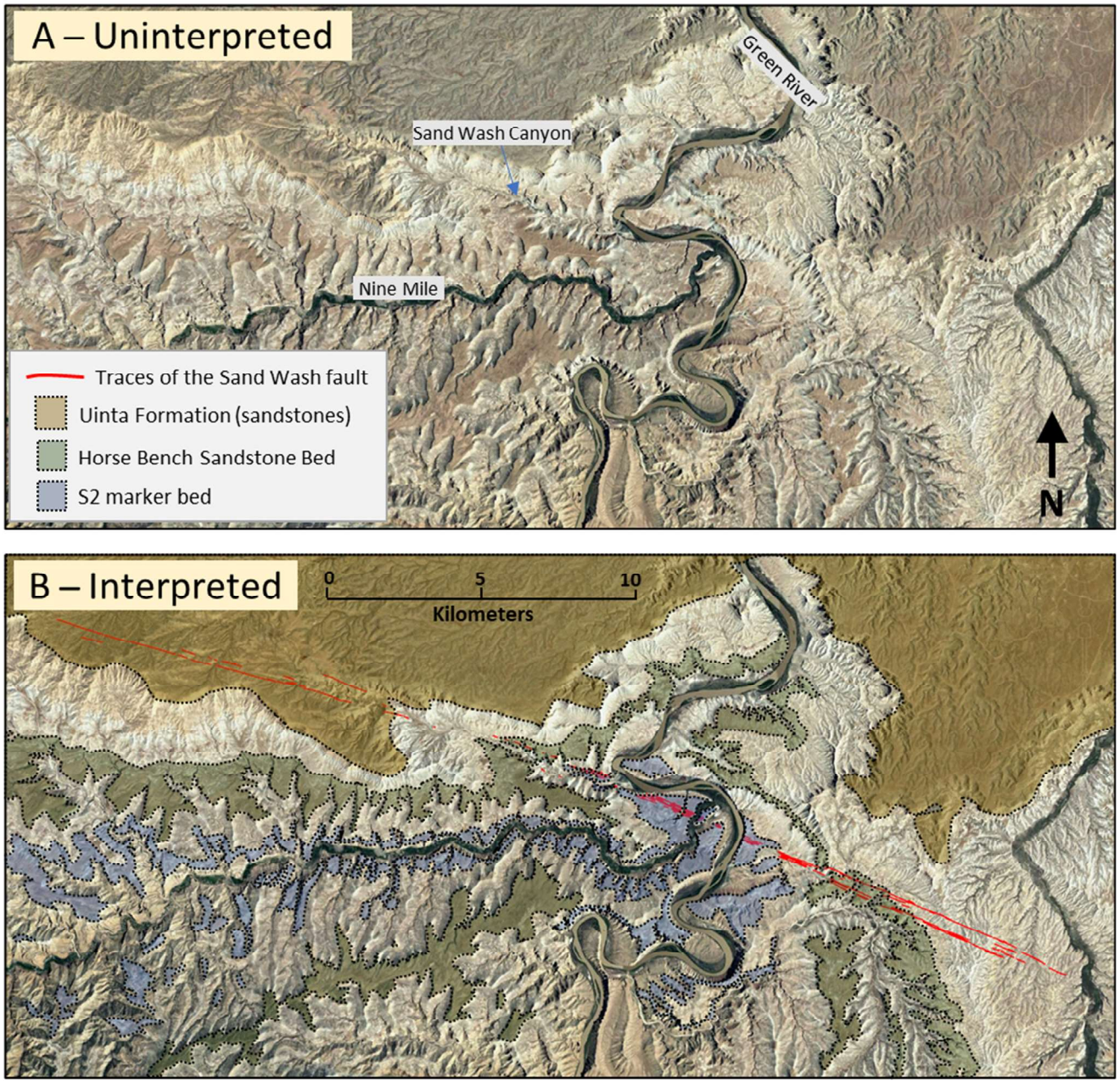

Figure 2. *Satellite images of the Sand Wash area of interest. A) Uninterpreted image, with the Green River running from north to south and Nine Mile Creek flowing into it from the west. Sand Wash Canyon is easily visible, forming along weaknesses created by the fault zone fracturing of the stratigraphic column. B) Same image with the fault zone outlined in red and the major brittle sandstone members highlighted.*

in this rapidly subsiding basin. The basin is longitudinally (W-E) asymmetric with a relatively narrow, steeply dipping northern limb adjacent to the thrusted southern margin of the Uinta Mountains, and a wide, gently dipping south limb stretching from the East and West Tavaputs Plateaus to the synclinal axis (Fouch, 1976; Fouch and others, 1994a; Ford and others, 2016) (figure 5). The SWFZ lies on the gently dipping southern limb of the Uinta Basin where the Green River and its tributaries have incised the Eocene Green River and Uinta Formations, creating classic Colorado Plateau mesa and slope topography (Remy, 1992) (figure 2).

The contemporaneous Paleocene-Eocene-aged fluvial Wasatch and Colton Formations were deposited during early basin development. This was followed by deposition of the lacustrine-dominated GRF as Lake Uinta expanded. The deepest part of the Uinta Basin accumulated approximately 6,000 meters of fluvial-lacustrine sediments over 10-million years (Davis and others, 2010). By the end of the Eocene, Lake Uinta finally disappeared as the fluvial-dominated Uinta and Duchesne River sediments progressively filled the basin from the east (Smith and others, 2008).

In the study area, the eastern part of the SWFZ

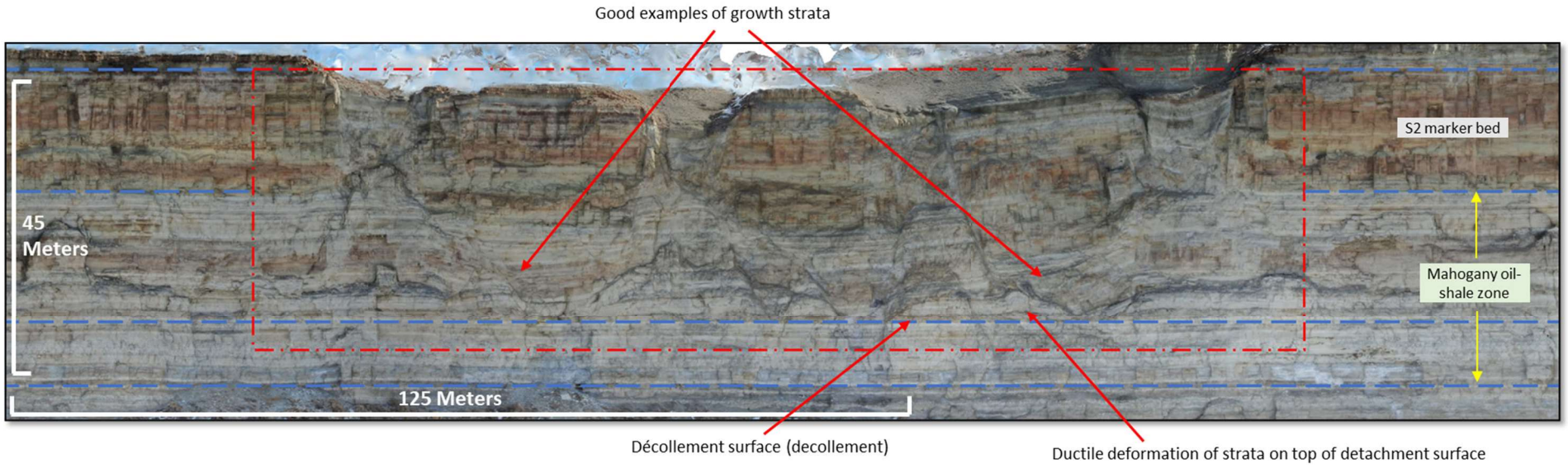

Figure 3. *East-southeast directed view at a cliff-face adjacent to the Green River consisting of the S2 marker bed and the Mahogany oil-shale zone of the Parachute Creek Member of the Green River Formation. The Sand Wash fault zone cuts perpendicularly through the outcrop, and here consists of a graben with three fault blocks (within the red box) that have foundered into the more ductile Mahogany. Note that the underlying stratigraphy is largely undisturbed. Image created in Agisoft Metashape™ using drone photography. This outcrop is particularly well-exposed, with easily identifiable strata and fault surfaces, allowing us to estimate total extension here. Measuring the cumulative length of identifiable strata within the fault zone divided by total width of the zone results in an estimate of 33.25 meters of total extension. This outcrop is listed as "Green River Pan Photo" on figure 4.*

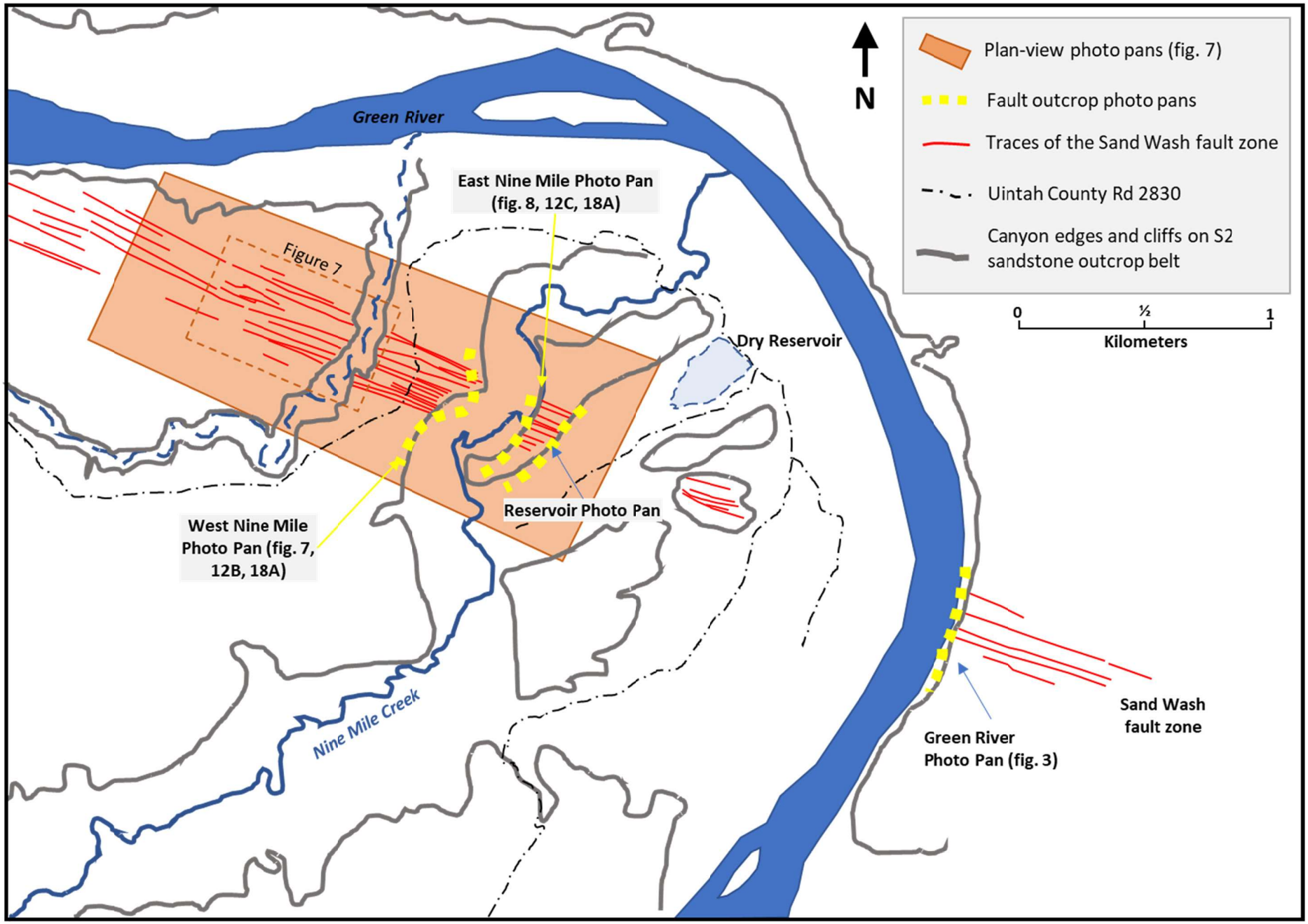

Figure 4. *Map of the study area showing the relation of the fault traces to the photo pans and figure locations. The canyon edges are shown because the best exposures of the fault zone and involved stratigraphy are visible there.*

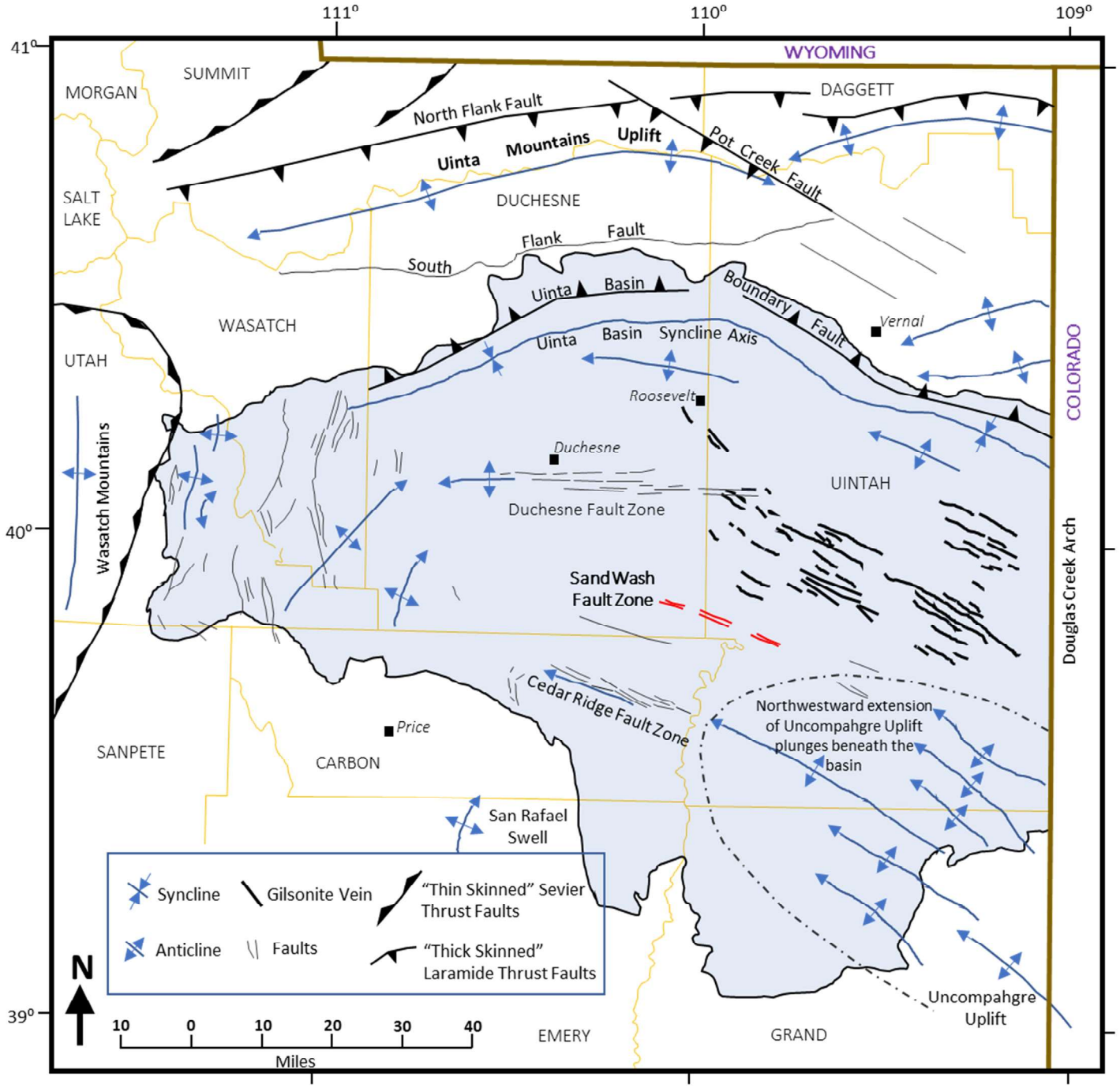

Figure 5. *Tectonic features of the Uinta Basin. Note the Sand Wash Fault Zone in red. Modified from Osmond, 1965 and Sprinkel, 2014. This map helps interpret the Sand Wash fault zone as neutral surface deformation associated with the extension on the outer arc of the Uncompahgre anticline, similar to the Cedar Ridge fault zone.*

cuts the Parachute Creek Member (including the informal S1 and S2 sandstone marker beds, and the formal Horse Bench Sandstone Bed), and the Sandstone and Limestone member of the GRF (figures 2 and 6); whereas the western part of the fault zone cuts the Sandstone and Limestone member of the GRF, and the overlying Uinta "B" member of the Uinta Formation. Here the mesa tops are held up by the relatively thin sandstone units of the Parachute Creek Member of the upper GRF, the Sandstone and Limestone member of the GRF, and the Uinta B member of the Uinta Formation. The slopes consist of argillaceous and organic-rich dolomite and siltstone beds of the Parachute Creek Member. The Parachute Creek Member type section is in the Piceance Basin of northwestern Colorado, and is mostly oil shale, marlstone, and tuff beds with minor siltstone and sandstone (Bradley, 1931). The Parachute Creek Member is well known for its kerogen-rich rocks, and includes the best developed, and most laterally continuous oil shale beds in both the Uinta and Piceance Basins. The most widespread, continuous, and best-known oil

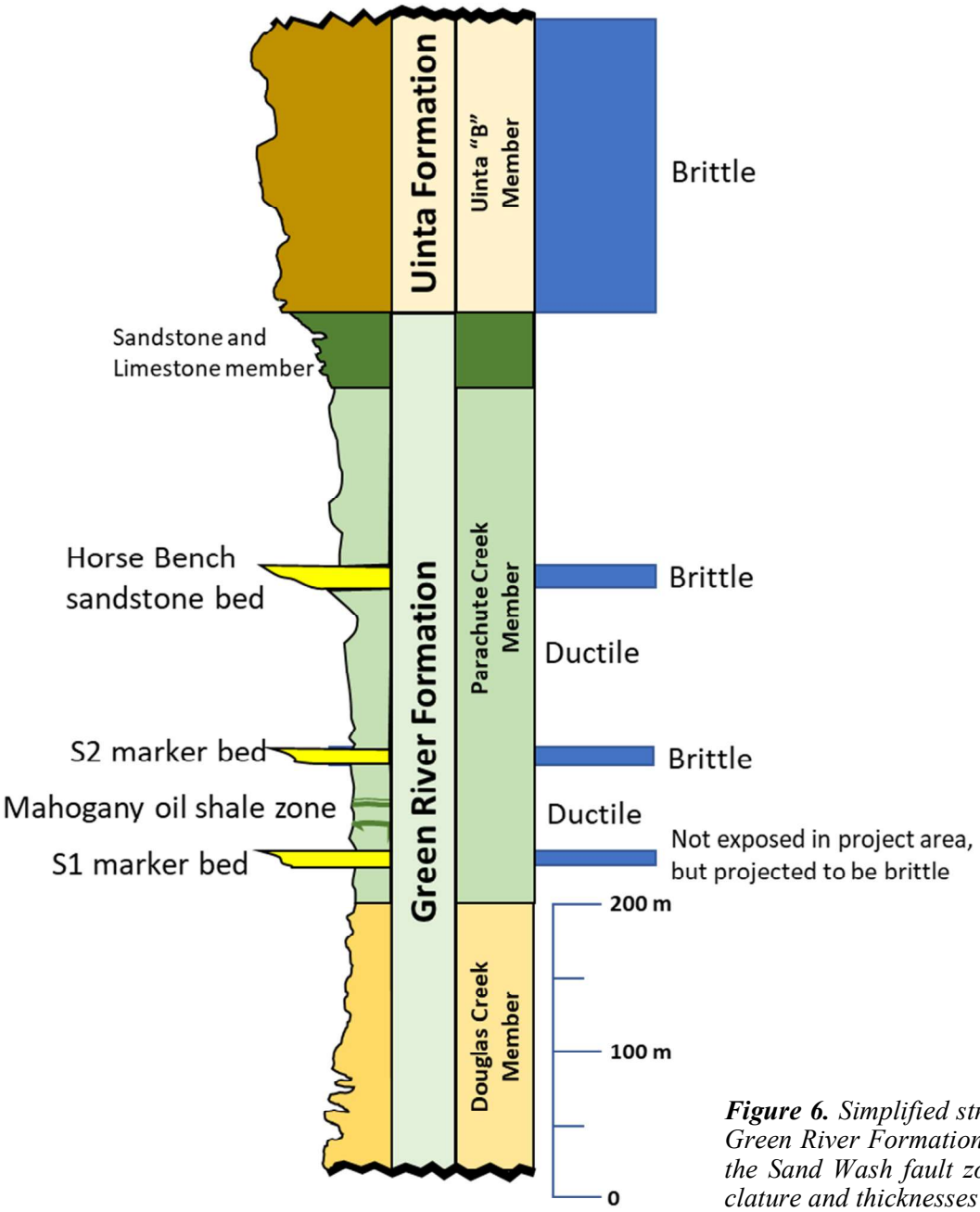

Figure 6. *Simplified stratigraphic column of the upper Green River Formation and lower Uinta Formation in the Sand Wash fault zone area. Stratigraphic nomenclature and thicknesses based on Remy, 1992.*

shale unit in the Parachute Creek Member is the Mahogany oil-shale zone, named for its resemblance to finished mahogany when polished (Bradley, 1931). The Mahogany oil-shale zone (MOSZ), or R7 zone (Birgenheier and Vanden Berg, 2011; Keighley and others, 2015) consists, in the study area, of about 30 meters of oil shale, argillaceous dolomite, and tuff beds. Cashion (1967) found that the Parachute Creek Member becomes progressively siltier and sandier towards the southern part of the Uinta Basin. In particular, the Parachute Creek Member in the study area contains many thin, laterally continuous siltstone and fine-grained sandstone beds, and three well-developed sheet sandstone beds. In ascending stratigraphic order, these sheet sandstone beds are the S1 and S2 sandstone marker beds, and the Horse Bench Sandstone bed (Fouch and others, 1976; Remy, 1992; Morgan, 2003; Keighley, 2013; Töro and Pratt, 2015). All three form prominent benches and mesas in the Sand Wash and Nine Mile Canyon areas. Cashion (1967) and Remy (1992) interpreted these as sheet sandstones deposited as shallow water lacustrine deltas that prograded into Lake Uinta from the south. They consist of classic coarsening upward sequences of fine-grained, tuffaceous sandstones with trough cross-bedding and hummocky beds. These sheet sandstone beds are intensely deformed in the SWFZ fault, whereas the intervening oil-shale-rich section is relatively undisturbed.

METHODS

The goal of the study was to map the magnitude and style of deformation associated with the SWFZ (figure 2) and create a structural model that best fits the observed deformation. Using photogrammetric models derived from panoramic photographs (photo pans) captured by unmanned aerial vehicles (UAVs, or drones), we measured the lengths and throws of fault segments as well as related deformation. We also used these photogrammetric models to measure the undeformed beds that are stratigraphically above and below fault segments. High-resolution photo pans were made of nine separate canyon wall exposures where the S2 sandstone marker bed is cut by the SWFZ. Also, a large plan-view photo pan of structural deformation of the S2 sandstone marker bed was interpreted, and comparisons were made to measurements made in the vertical outcrops. Orientations of fault surfaces were measured in the S2 sandstone marker bed, Horse Bench Sandstone Bed, and Uinta B member, as were joint sets in each sedimentary unit. These measurements are presented in tables 1 through 7. The fault surface measurements were plotted on equal-angle stereographic projections. Fault strike and dips were then identified by formation and differences measured. Slickenline directions were also measured and slickenline overprint relationships noted (figure 7). Projections of slickenline directions were plotted as stereographs with interpreted overprinting relationships and related to regional tectonics. Folds were noted, and the long axis and direction of shear were measured. Décollement surfaces were observed, and their width, lithology, and sense of shear measured. Pervasive soft-sediment deformation features such as flame structures and ball and pillows were observed, with locations, stratigraphic unit, and lithologies recorded. Sedimentary features such as growth strata, debrites, missing strata, and rafts were noted and photographed.

Fault lengths and geometries - We measured individual fault traces using satellite imagery from Google Earth Pro™ and drone photogrammetry, using a Mavic 2 Zoom™ drone with a 12-megapixel camera stabilized on a 3-axis gimbal; the photographs were used to create a 3D photorealistic model using Agisoft™ Metashape software (figure 8). Each photogrammetry model typically involved 200 to 500 photographs taken 50 to 100 meters from the outcrop face. Individual fault strands (traces) were defined as through-going ruptures measured from tip to tip. Faults connected through relay ramps were measured as separate faults. Individual lengths were measured digitally, and the involved stratigraphic units noted (table 1). Limitations of this method include the underestimation of strand lengths due to lack of completely visible surface rupture (covered by regolith, soil, vegetation) and complicated topography limiting outcrop exposures, such as a faulted rock unit being cut by a steep-walled canyon. In ambiguous cases, we measured to the edge of the visible strand, choosing to underestimate fault lengths.

Fault displacements - Fault displacements were measured on individual segments where marker beds were offset on high, vertical cliffs bordering Nine Mile Creek and the Green River (figure 9). Global Positioning System-referenced (GPS) photographs of the cliff faces were then used to build large 3D models and measure offsets using Agisoft™ software. Offset measurements should be considered apparent measurements on the vertical cliff faces because oblique and strike-slip movement are not visible. Displacement magnitude of individual segments often changed along the dip length of the fault. Rather than attempting to capture changing displacement magnitudes through multiple measurements on a single fault strand, we instead took a single measurement on the most easily identifiable offset marker bed. A total of 110 stratigraphic strike and dips were collected within the SWFZ, as well as south and north of the zone. Displacement data is collected in table 2.

Fault plane orientations - Individual fault-plane orientation data were collected for as many surfaces in the Uinta Formation, Horse Bench Sandstone Bed, and S2 sandstone marker beds as we could access (figure 7). The dataset is weighted heavily toward the sandstones as preserved fault surfaces suitable for orientation measurements are not found within the shales. The measurements (tables 3A, B, and C) and their accompanying stereographs (figures 10A, B, and C) are listed by stratigraphic intervals.

Slickenlines - We measured slickenlines on fault surfaces to determine fault slip orientations and distinguish between mode 1, 2, and 3 fractures (tables 4A, B, and C; figures 11A, B, and C). Slickenlines plot as points on a great circle, which represents the fault plane. Depending on the dip of the fault, slickenline plunges can help determine the amount of strike slip vs. dip slip (figure 11D). However, sense of shear is difficult to determine from slickenline data alone and requires identifying the direction a marker is offset.

Measuring fault zone extension - To measure total extension across the fault zone, detailed length measurements were made on the top of the S2 marker bed on the grabens and other identifiable blocks, then this sum was subtracted from the total width of the fault zone. The cleanest measurements were made on the cliff-face shown on figure 3.

Fracture data – Joints and fractures were measured within and adjacent to the fault zone in multiple

Table 1. *Fault segment length by stratigraphic unit in meters.*

Uinta Formation	Sandstone and Limestone Facies	Horse Bench	Parachute Creek Shales and Siltstones	S2
Average length in meters				
1421	177	406	781	303
429	149	287	685	323
345		375	491	330
434		383	401	317
432		925	252	215
209		642	280	112
158		513	231	157
277		72	408	99
175		31	167	235
543		9	296	259
26		6	150	268
248		250	246	150
308		72	1558	289
140		186	408	155
280		116	1584	111
288		222	520	113
941		38	1096	67
604		111	271	104
363			734	106
197			483	91
477			1039	114
57			135	84
289			150	67
159			393	197
116			208	217
118			90	79
447			81	149
339			235	156
144			119	478
479			1618	522
1481			975	512
791			1079	147
682			758	254
19			336	202
199			99	174
			86	303
			195	435
			98	97
			148	408
			248	80
			129	140
			222	224
			203	66
			380	91

Table 1 continued. *Fault segment length by stratigraphic unit in meters.*

Uinta Formation	Sandstone and Limestone Facies	Horse Bench	Parachute Creek Shales and Siltstones	S2
Average length in meters				
			887	208
			296	331
			475	301
			780	305
			443	297
			332	184
			93	248
			134	184
			169	538
			320	449
			110	296
			106	352
			854	303
			208	237
			63	399
			153	444
			254	295
			588	301
			125	183
			59	103
			74	125
			162	177
			65	107
			206	69
			228	227
			179	64
			25	72
			95	103
			279	18
			127	13
			149	49
			77	91
			138	58
			94	67
			181	48
			78	71
				85
				90
				76
				105
				92
				129
Average Segment Lengths				159
389	***163***	***258***	***358***	***196***

Table 2. *Displacements on discreet fault segments in meters. Locations noted on figure 4.*

Segment	Offset (m)
North Face Nine Mile Mahogany Zone	2.96
North Face Nine Mile Mahogany Zone	2.85
North Face Nine Mile Mahogany Zone	3.04
North Face Nine Mile Mahogany Zone	0.53
North Face Nine Mile Mahogany Zone	0.46
North Face Nine Mile Mahogany Zone	0.79
North Face Nine Mile Mahogany Zone	0.51
North Face Nine Mile Mahogany Zone	3.81
North Face Nine Mile Mahogany Zone	4.94
North Face Nine Mile S2 Sandstone	0.51
North Face Nine Mile S2 Sandstone	0.65
North Face Nine Mile S2 Sandstone	1.64
North Face Nine Mile S2 Sandstone	3.66
North Face Nine Mile S2 Sandstone	3.14
North Face Nine Mile S2 Sandstone	1.79
North Face Reservoir Cliff S2 Sandstone	0.51
North Face Reservoir Cliff S2 Sandstone	2.91
Ranger Cliff S2 Sandstone	1.24
Ranger Cliff S2 Sandstone	1.16
Ranger Cliff S2 Sandstone	0.72
Ranger Cliff S2 Sandstone	0.77
Ranger Cliff S2 Sandstone	0.79
Ranger Cliff S2 Sandstone	0.33
Ranger Cliff S2 Sandstone	0.35

Segment	Offset (m)
South Face Nine Mile S2 Sandstone	1.07
South Face Nine Mile S2 Sandstone	1.99
South Face Nine Mile S2 Sandstone	1.42
South Face Nine Mile S2 Sandstone	1.58
South Face Nine Mile S2 Sandstone	1.90
South Face Nine Mile S2 Sandstone	1.29
South Face Nine Mile S2 Sandstone	0.58
South Face Nine Mile S2 Sandstone	1.63
South Face Nine Mile S2 Sandstone	0.75
South Face Nine Mile S2 Sandstone	4.68
South Face Nine Mile S2 Sandstone	2.11
South Face Nine Mile S2 Sandstone	2.31
South Face Nine Mile S++++2 Sandstone	2.48
South Face Nine Mile S2 Sandstone	1.17
South Face Nine Mile S2 Sandstone	1.23
South Face Nine Mile S2 Sandstone	1.13
South Face Nine Mile S2 Sandstone	2.02
South Face Nine Mile S2 Sandstone	3.09
South Face Nine Mile S2 Sandstone	1.02
South Face Nine Mile S2 Sandstone	0.89
South Face Nine Mile S2 Sandstone	0.87
South Face Nine Mile S2 Sandstone	0.60
South Face Nine Mile S2 Sandstone	0.55
South Face Nine Mile S2 Sandstone	0.60

Segment	Offset (m)
South Face Nine Mile Mahogany Zone	0.278
South Face Nine Mile Mahogany Zone	0.879
South Face Nine Mile Mahogany Zone	0.713
South Face Nine Mile Mahogany Zone	1.120
South Face Nine Mile Mahogany Zone	1.580
South Face Nine Mile Mahogany Zone	0.782
South Face Nine Mile Mahogany Zone	0.762
South Face Nine Mile Mahogany Zone	1.420
South Face Nine Mile Mahogany Zone	1.280
South Face Nine Mile Mahogany Zone	1.210
South Face Nine Mile Mahogany Zone	0.390
South Face Nine Mile Mahogany Zone	0.232
South Face Nine Mile Mahogany Zone	1.230
South Face Nine Mile Mahogany Zone	0.606
South Face Nine Mile Mahogany Zone	2.040
South Face Nine Mile Mahogany Zone	1.630
South Face Nine Mile Mahogany Zone	1.210
South Face Nine Mile Mahogany Zone	2.460
South Face Nine Mile Mahogany Zone	0.507
South Face Nine Mile Mahogany Zone	0.266
South Face Nine Mile Mahogany Zone	0.369

Table 2 continued. *Displacements on discreet fault segments in meters. Locations noted on figure 4.*

Segment	Offset (m)
Ranger Cliff S2 Sandstone	0.87
Ranger Cliff S2 Sandstone	0.21
Ranger Cliff S2 Sandstone	0.16
Ranger Cliff S2 Sandstone	0.69
Ranger Cliff S2 Sandstone	0.82
Ranger Cliff S2 Sandstone	0.20
Green River S2 Sandstone	4.49

Segment	Offset (m)
South Face Nine Mile S2 Sandstone	1.05
South Face Nine Mile S2 Sandstone	1.19
South Face Nine Mile S2 Sandstone	2.85
South Face Nine Mile S2 Sandstone	3.14
South Face Nine Mile S2 Sandstone	0.49
South Face Nine Mile S2 Sandstone	1.15
South Face Nine Mile S2 Sandstone	0.30
South Face Nine Mile S2 Sandstone	0.43
South Face Nine Mile S2 Sandstone	0.62
South Face Nine Mile S2 Sandstone	0.96
South Face Nine Mile S2 Sandstone	0.48
South Face Nine Mile S2 Sandstone	0.58
South Face Nine Mile S2 Sandstone	1.54
South Face Nine Mile S2 Sandstone	1.24
South Face Nine Mile S2 Sandstone	0.92
South Face Nine Mile S2 Sandstone	1.13
South Face Nine Mile S2 Sandstone	1.33

Segment	Offset (m)

***Table 3A**. Fault surface dips, dip directions and locations for the Uinta Formation.*

No.	Dip	Direction	Latitude	Longitude	Description
1	72.384	179.303	39.86279	-110.01883	Fault Surface Uinta Formation
2	82.466	185.824	39.86281	-110.01886	Fault Surface Uinta Formation
3	84.881	8.261	39.86277	-110.01886	Fault Surface Uinta Formation
4	83.200	185.233	39.86276	-110.01890	Fault Surface Uinta Formation
5	64.297	180.588	39.86269	-110.01890	Fault Surface Uinta Formation
7	80.726	192.734	39.86034	-110.00895	Fault Surface Uinta Formation
8	70.863	194.741	39.86034	-110.00898	Fault Surface Uinta Formation

***Table 3B.** Fault surface dips, dip directions and locations for the Horse Bench Sandstone.*

No.	Dip	Direction	Latitude	Longitude	Description
1	80.692	356.616	39.86660	-110.02669	Horse Bench Fault Surface
2	88.563	180.257	39.84290	-109.93847	Horse Bench Fault Surface
3	78.025	210.332	39.84292	-109.93833	Horse Bench Fault Surface
4	63.945	185.552	39.84278	-109.93814	Horse Bench Fault Surface
5	87.849	194.215	39.84274	-109.93827	Horse Bench Fault Surface
6	88.904	171.052	39.84278	-109.93840	Horse Bench Fault Surface
7	40.488	190.367	39.84279	-109.93840	Horse Bench Fault Surface
8	82.281	14.579	39.84324	-109.93311	Horse Bench Fault Surface
9	85.731	197.694	39.84322	-109.93311	Horse Bench Fault Surface
10	82.468	193.080	39.84359	-109.93305	Horse Bench Fault Surface
11	77.350	190.913	39.84367	-109.93303	Horse Bench Fault Surface
12	82.615	199.038	39.84371	-109.93290	Horse Bench Fault Surface
13	83.712	192.020	39.84379	-109.93291	Horse Bench Fault Surface
14	87.182	194.844	39.84991	-109.95252	Horse Bench Fault Surface
15	88.546	194.801	39.84993	-109.95251	Horse Bench Fault Surface

***Table 3C.** Fault surface dips, dip directions and locations for the S2 marker bed.*

No.	Dip	Direction	Latitude	Longitude	Description
1	81.285	13.099	39.84030	-109.92578	S2 Sandstone Fault Surface
2	86.870	180.024	39.84033	-109.92578	S2 Sandstone Fault Surface
3	68.022	357.486	39.84034	-109.92581	S2 Sandstone Fault Surface
4	75.525	176.659	39.84039	-109.92580	S2 Sandstone Fault Surface
5	76.090	182.331	39.84044	-109.92572	S2 Sandstone Fault Surface
6	40.994	183.469	39.84039	-109.92571	S2 Sandstone Fault Surface
7	84.864	3.470	39.84040	-109.92573	S2 Sandstone Fault Surface
8	89.074	9.551	39.84096	-109.92693	S2 Sandstone Fault Surface
9	88.572	9.298	39.84018	-109.92542	S2 Sandstone Fault Surface
10	83.592	189.304	39.84018	-109.92542	S2 Sandstone Fault Surface
11	83.119	2.651	39.84022	-109.92540	S2 Sandstone Fault Surface
12	65.824	181.611	39.84023	-109.92541	S2 Sandstone Fault Surface
13	88.299	186.171	39.84041	-109.92465	S2 Sandstone Fault Surface
14	87.478	8.316	39.84000	-109.92434	S2 Sandstone Fault Surface
15	78.931	10.628	39.83997	-109.92423	S2 Sandstone Fault Surface
16	70.873	201.065	39.83995	-109.92333	S2 Sandstone Fault Surface
17	71.024	198.044	39.83990	-109.92272	S2 Sandstone Fault Surface
18	87.045	198.184	39.82795	-109.88863	S2 Sandstone Fault Surface
19	82.093	197.350	39.82796	-109.88860	S2 Sandstone Fault Surface
20	82.219	194.572	39.82806	-109.88857	S2 Sandstone Fault Surface
21	89.207	196.059	39.82532	-109.90097	S2 Sandstone Fault Surface
22	76.606	22.641	39.84000	-109.92434	S2 Sandstone Fault Surface
23	85.782	184.642	39.83997	-109.92423	S2 Sandstone Fault Surface
24	68.810	1.495	39.83995	-109.92333	S2 Sandstone Fault Surface
25	76.841	188.139	39.83990	-109.92272	S2 Sandstone Fault Surface
26	77.431	186.123	39.84039	-109.92571	S2 Sandstone Fault Surface
27	77.354	192.162	39.84040	-109.92573	S2 Sandstone Fault Surface
28	83.765	188.335	39.84096	-109.92693	S2 Sandstone Fault Surface
29	43.218	181.775	39.84018	-109.92542	S2 Sandstone Fault Surface
30	84.986	2.462	39.84018	-109.92542	S2 Sandstone Fault Surface
31	77.971	8.853	39.84022	-109.92540	S2 Sandstone Fault Surface
32	81.191	17.227	39.84018	-109.92542	S2 Sandstone Fault Surface
33	66.003	26.050	39.84022	-109.92540	S2 Sandstone Fault Surface
34	71.120	227.519	39.84023	-109.92541	S2 Sandstone Fault Surface
35	65.407	170.765	39.84041	-109.92465	S2 Sandstone Fault Surface
36	71.900	184.363	39.84000	-109.92434	S2 Sandstone Fault Surface
37	84.865	176.323	39.83997	-109.92423	S2 Sandstone Fault Surface
38	86.555	195.934	39.83995	-109.92333	S2 Sandstone Fault Surface
39	73.094	205.523	39.84030	-109.92578	S2 Sandstone Fault Surface
40	67.708	213.780	39.84033	-109.92578	S2 Sandstone Fault Surface
41	71.635	203.688	39.84034	-109.92581	S2 Sandstone Fault Surface
42	87.267	19.747	39.84039	-109.92580	S2 Sandstone Fault Surface

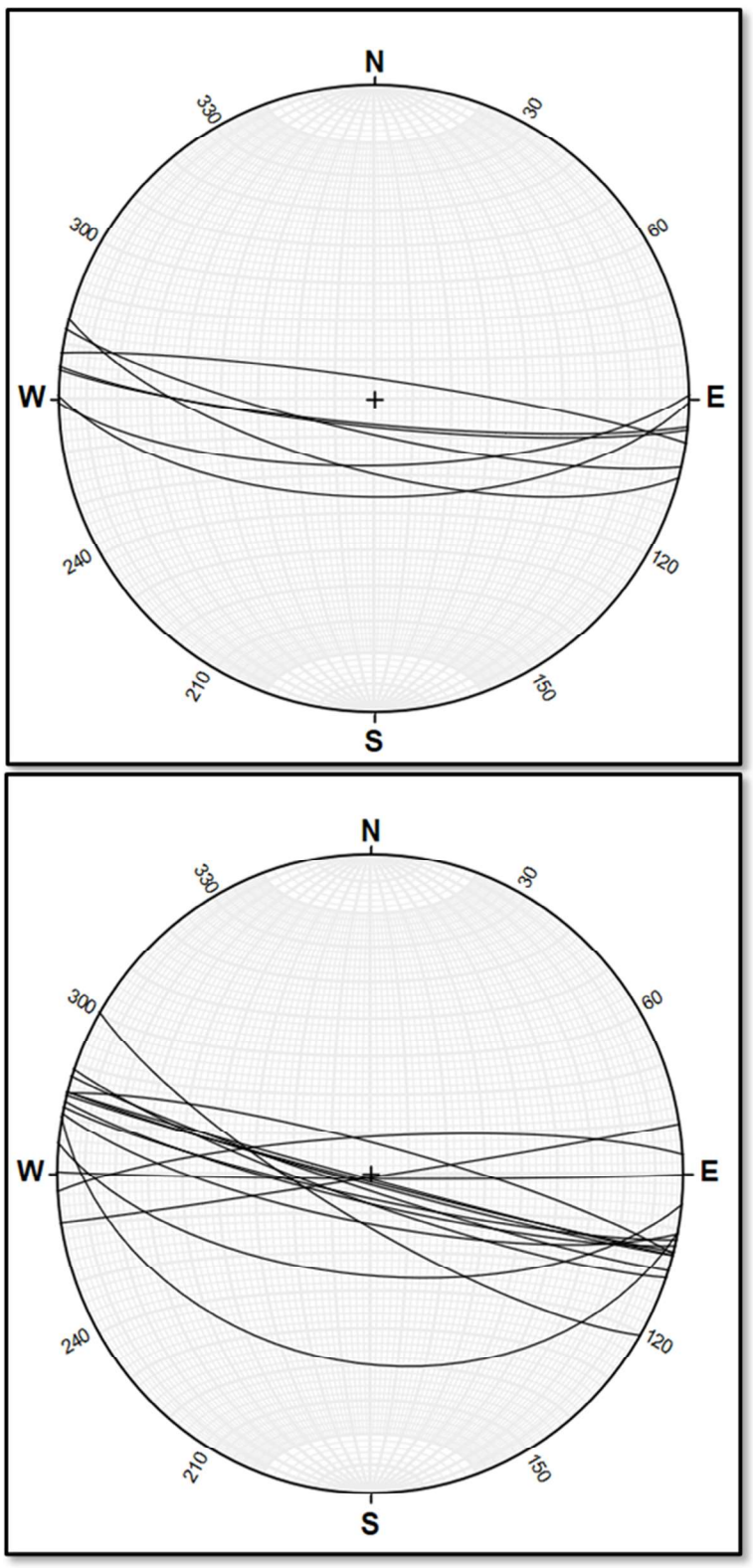

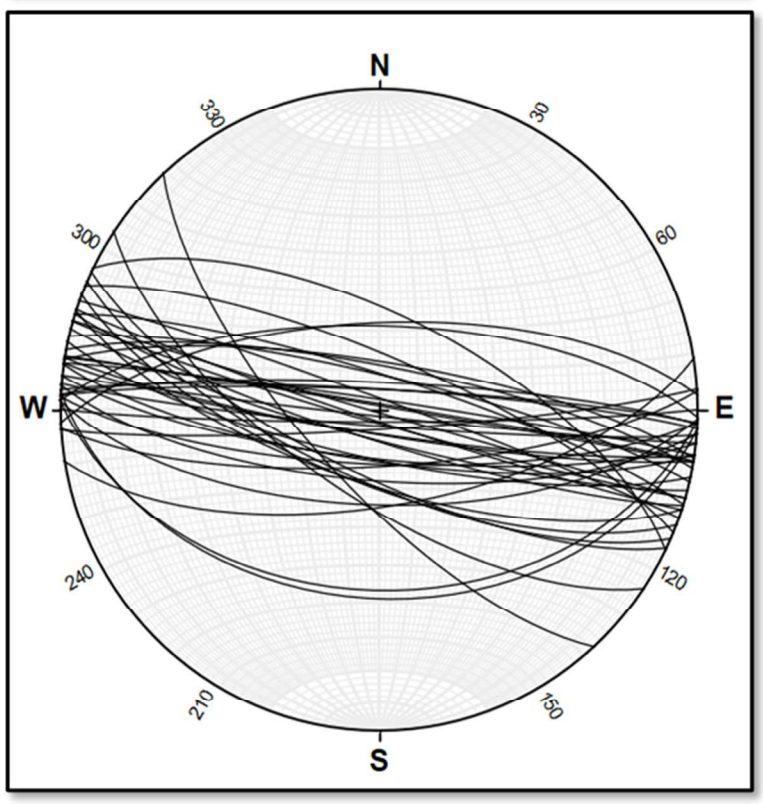

Table 4A. *Fault surface slickenlines plunges, trends, and locations for the Uinta Formation.*

No.	Plunge	Trend	Latitude	Longitude	Description
1	76.389	202.952	39.86045	-110.00896	Uinta Formation Slickenlines
2	60.567	204.556	39.86035	-110.00895	Uinta Formation Slickenlines

Table 4B. *Fault surface slickenlines plunges, trends and locations for the Horse Bench Sandstone.*

No.	Plunge	Trend	Latitude	Longitude	Description
1	83.079	92.390	39.84290	-109.93845	Horse Bench Sandstone Slickenlines
2	74.511	160.314	39.84291	-109.93841	Horse Bench Sandstone Slickenlines
3	37.365	193.586	39.84279	-109.93840	Horse Bench Sandstone Slickenlines
4	83.308	203.815	39.84363	-109.93300	Horse Bench Sandstone Slickenlines

Table 4C. *Fault surface slickenlines plunges, trends, and locations for the S2 marker bed.*

No.	Plunge	Trend	Latitude	Longitude	Description
1	82.511	14.050	39.84025	-109.92577	S2 Sandstone Slickenlines
2	80.665	254.598	39.84032	-109.92581	S2 Sandstone Slickenlines
3	69.768	15.264	39.84036	-109.92581	S2 Sandstone Slickenlines
4	53.484	123.536	39.84039	-109.92580	S2 Sandstone Slickenlines
5	48.188	261.357	39.84039	-109.92567	S2 Sandstone Slickenlines
6	11.191	100.558	39.84047	-109.92573	S2 Sandstone Slickenlines
7	80.359	279.167	39.84041	-109.92571	S2 Sandstone Slickenlines
8	16.490	100.278	39.84041	-109.92574	S2 Sandstone Slickenlines
9	40.573	207.521	39.84041	-109.92572	S2 Sandstone Slickenlines
10	81.376	310.956	39.84036	-109.92580	S2 Sandstone Slickenlines
11	25.873	273.056	39.84096	-109.92692	S2 Sandstone Slickenlines
12	76.719	84.124	39.84017	-109.92546	S2 Sandstone Slickenlines
13	81.135	139.298	39.84019	-109.92542	S2 Sandstone Slickenlines
14	75.171	67.197	39.84022	-109.92542	S2 Sandstone Slickenlines
15	63.010	209.098	39.84047	-109.92502	S2 Sandstone Slickenlines
16	85.911	15.658	39.84001	-109.92433	S2 Sandstone Slickenlines
17	79.134	63.082	39.84002	-109.92420	S2 Sandstone Slickenlines
18	69.974	178.751	39.83983	-109.92230	S2 Sandstone Slickenlines
19	63.976	149.381	39.83990	-109.92265	S2 Sandstone Slickenlines
20	71.025	193.375	39.83992	-109.92271	S2 Sandstone Slickenlines
21	79.031	13.090	39.84025	-109.92577	S2 Sandstone Slickenlines
22	84.353	227.440	39.84032	-109.92581	S2 Sandstone Slickenlines
23	68.509	351.964	39.84036	-109.92581	S2 Sandstone Slickenlines
24	65.108	133.470	39.84039	-109.92580	S2 Sandstone Slickenlines
25	50.990	260.051	39.84039	-109.92567	S2 Sandstone Slickenlines
26	20.623	105.765	39.84047	-109.92573	S2 Sandstone Slickenlines
27	73.637	255.204	39.84041	-109.92571	S2 Sandstone Slickenlines
28	35.629	206.352	39.84041	-109.92574	S2 Sandstone Slickenlines
29	80.763	307.453	39.84041	-109.92572	S2 Sandstone Slickenlines
30	78.115	19.629	39.84036	-109.92580	S2 Sandstone Slickenlines
31	73.596	323.888	39.84096	-109.92692	S2 Sandstone Slickenlines
32	51.489	334.844	39.84017	-109.92546	S2 Sandstone Slickenlines
33	73.210	231.848	39.84019	-109.92542	S2 Sandstone Slickenlines
34	63.859	187.747	39.84036	-109.92580	S2 Sandstone Slickenlines
35	66.786	161.159	39.84096	-109.92692	S2 Sandstone Slickenlines
36	71.981	102.942	39.84017	-109.92546	S2 Sandstone Slickenlines
37	77.325	272.248	39.84019	-109.92542	S2 Sandstone Slickenlines
38	74.354	183.486	39.84022	-109.92542	S2 Sandstone Slickenlines
39	68.308	213.338	39.84047	-109.92502	S2 Sandstone Slickenlines
40	64.657	246.603	39.84001	-109.92433	S2 Sandstone Slickenlines
41	84.143	315.541	39.84002	-109.92420	S2 Sandstone Slickenlines
42	79.783	52.374	39.82979	-109.89087	S2 Sandstone Slickenlines

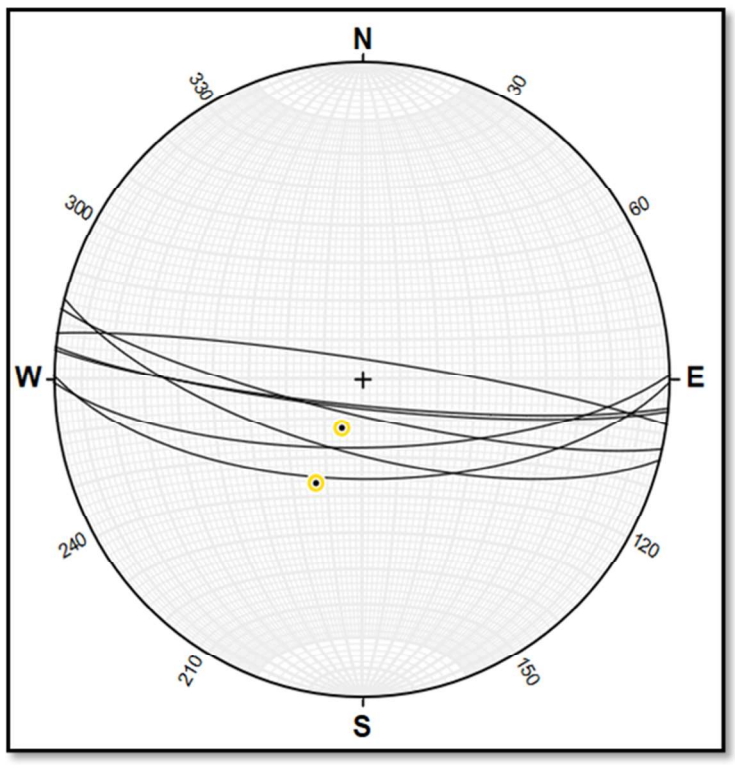

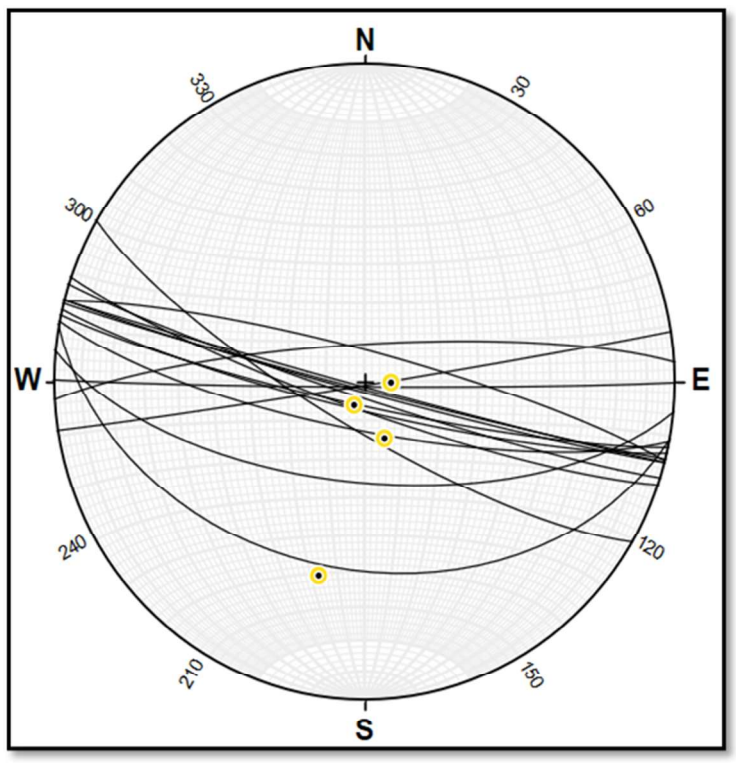

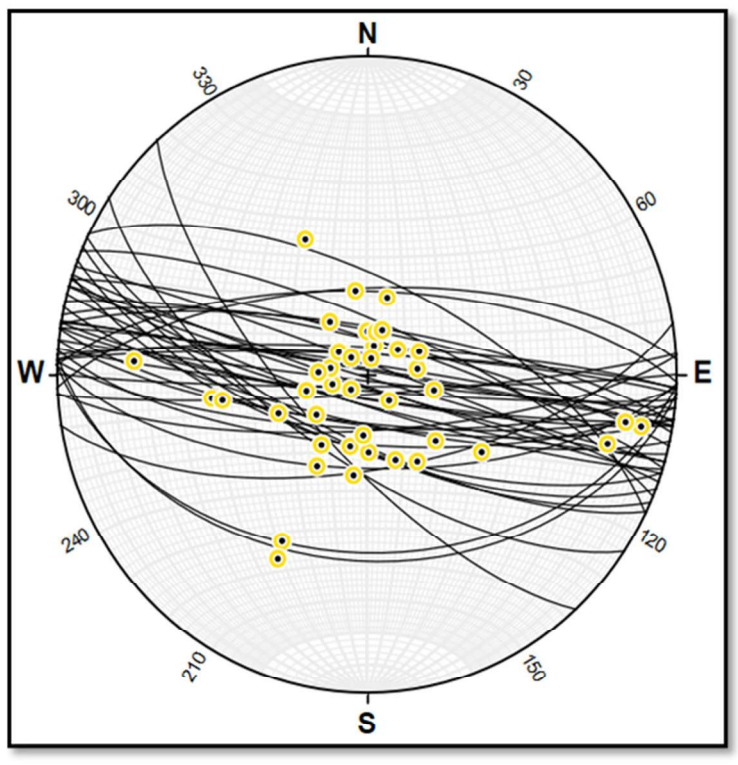

Table 5. *Joint dips, dip directions, and locations in the Sand Wash fault zone.*

No.	Dip	Dip Direction	Latitude	Longitude
1	80.243	196.487	39.83955	-109.92321
2	83.340	195.890	39.84271	-109.93977
3	80.229	191.291	39.84300	-109.93861
4	89.073	11.198	39.84006	-109.92400
5	73.444	13.687	39.83997	-109.92439
6	90.000	16.630	39.84027	-109.92453
7	89.284	190.383	39.84039	-109.92478
8	84.069	193.202	39.84299	-109.93855
9	82.940	216.945	39.83963	-109.92251
10	88.455	30.303	39.83963	-109.92257
11	88.522	24.786	39.83960	-109.92256
12	84.609	208.170	39.83959	-109.92256
13	90.000	25.513	39.83959	-109.92257
14	90.000	205.352	39.83958	-109.92256
15	77.241	208.593	39.83965	-109.92253
16	83.807	215.985	39.83965	-109.92252
17	76.895	205.591	39.83965	-109.92249
18	90.000	218.059	39.83965	-109.92246

Table 6. *Fold axial-plane dip and dip direction data defining the axial surface of folds in the Mahogany bed and the lower S2 marker bed.*

No.	Dip	Dip Direction	Latitude	Longitude	Formation
1	55.714	43.667	39.84095	-109.92696	S2 Fold
2	87.086	214.897	39.84019	-109.92586	S2 Fold
3	81.729	31.931	39.84017	-109.92588	S2 Fold
4	85.371	254.174	39.84009	-109.92590	S2 Fold
5	87.181	328.544	39.84009	-109.92575	S2 Fold
6	87.120	324.188	39.84011	-109.92574	S2 Fold
7	77.799	287.345	39.82982	-109.89084	S2 Fold
8	87.926	178.509	39.83971	-109.92275	S2 Fold
9	87.288	174.721	39.83967	-109.92272	S2 Fold
10	88.729	91.927	39.83962	-109.92246	S2 Fold
11	70.027	10.081	39.82930	-109.89060	Mahogany Fold
12	75.198	49.230	39.82982	-109.89077	Mahogany Fold
13	68.500	196.440	39.82882	-109.88923	Mahogany Fold
14	88.620	190.380	39.82833	-109.88849	Mahogany Fold
15	79.420	11.220	39.83962	-109.92246	Mahogany Fold
16	82.470	205.350	39.82869	-109.88786	Mahogany Fold
17	84.660	216.820	39.84299	-109.93855	Mahogany Fold
18	62.530	25.160	39.83963	-109.92251	Mahogany Fold

Table 7. *Stratigraphic dips, dip directions, and location data across the SWFZ. The steepest dips are within the fault zone on rotated blocks, and then steeper dips north of the fault zone than to the south.*

No.	Dip	Direction	Latitude	Longitude	No.	Dip	Direction	Latitude	Longitude	No.	Dip	Direction	Latitude	Longitude
1	5.7	328.9	39.87177	-110.02896	38	4.8	321.3	39.83752	-109.96163	75	6.1	355.2	39.82793	-109.88732
2	5.6	330.9	39.86555	-110.02527	39	4.4	277.5	39.83727	-109.95294	76	9.0	25.2	39.82782	-109.88749
3	11.5	172.7	39.86278	-110.01887	40	3.2	345.2	39.82805	-109.90356	77	2.1	258.4	39.82742	-109.88776
4	6.4	347.7	39.86296	-110.01891	41	3.9	331.5	39.82566	-109.89304	78	5.6	2.2	39.82717	-109.88795
5	5.4	301.4	39.86049	-110.00521	42	2.5	1.5	39.82661	-109.89144	79	6.6	14.8	39.82688	-109.88813
6	3.1	17.8	39.84781	-109.96855	43	3.6	16.8	39.82689	-109.89094	80	6.1	342.5	39.82665	-109.88833
7	2.8	327.7	39.84761	-109.96844	44	1.4	144.1	39.82720	-109.89015	81	4.0	46.1	39.82642	-109.88856
8	2.5	108.6	39.84709	-109.96909	45	5.7	357.0	39.82730	-109.88991	82	6.3	11.3	39.82637	-109.88862
9	2.5	79.1	39.84620	-109.97044	46	13.3	21.5	39.82746	-109.88932	83	3.6	299.9	39.82661	-109.88946
10	3.7	13.6	39.84758	-109.97157	47	6.5	23.1	39.82752	-109.88919	84	3.2	297.1	39.82537	-109.90064
11	2.7	340.9	39.84715	-109.97254	48	7.0	66.9	39.82760	-109.88898	85	2.9	316.9	39.83048	-109.92933
12	1.7	355.0	39.84770	-109.97124	49	25.1	5.8	39.82771	-109.88879	86	8.2	30.9	39.84822	-109.95862
13	3.9	23.9	39.84837	-109.96820	50	9.3	351.6	39.82809	-109.88852	87	5.7	32.3	39.84501	-109.94627
14	3.8	31.1	39.84900	-109.96706	51	3.8	225.8	39.82899	-109.88811	88	4.3	319.1	39.84208	-109.94062
15	2.2	0.2	39.84904	-109.96687	52	7.0	51.7	39.82939	-109.88819	89	4.5	1.1	39.83950	-109.93801
16	5.7	326.5	39.84908	-109.96583	53	1.0	318.9	39.83116	-109.88920	90	1.3	222.1	39.83886	-109.92269
17	9.1	8.1	39.84925	-109.96097	54	3.6	1.9	39.83213	-109.88776	91	6.2	47.5	39.83882	-109.92290
18	6.3	0.9	39.84941	-109.96118	55	0.7	42.7	39.83269	-109.88658	92	4.4	310.3	39.83880	-109.92303
19	6.6	42.0	39.85034	-109.96109	56	2.2	146.7	39.83275	-109.88581	93	2.2	71.6	39.83861	-109.92324
20	6.6	10.7	39.85035	-109.96105	57	2.8	331.4	39.83205	-109.88003	94	7.1	297.1	39.83913	-109.92337
21	4.4	345.1	39.85256	-109.95942	58	0.8	83.6	39.83235	-109.87995	95	1.9	49.5	39.83903	-109.92423
22	2.1	45.8	39.85270	-109.95922	59	3.9	81.1	39.83263	-109.88064	96	1.6	130.3	39.83908	-109.92528
23	2.0	61.4	39.85358	-109.95868	60	5.5	218.9	39.83214	-109.88238	97	1.0	115.6	39.83941	-109.92324
24	2.1	3.1	39.85462	-109.95817	61	2.8	337.1	39.83203	-109.88264	98	1.7	300.4	39.83952	-109.92275
25	1.2	57.1	39.85479	-109.95815	62	5.2	348.1	39.83200	-109.88312	99	10.0	89.7	39.83961	-109.92260
26	4.8	317.8	39.85424	-109.95937	63	4.9	48.6	39.83193	-109.88336	100	10.2	113.0	39.83965	-109.92250
27	2.1	331.3	39.85455	-109.96109	64	4.6	50.3	39.83187	-109.88340	101	2.7	89.1	39.84008	-109.92203
28	2.5	13.4	39.85451	-109.96131	65	2.7	310.6	39.83181	-109.88379	102	9.6	172.8	39.84019	-109.92188
29	3.3	357.7	39.85303	-109.96233	66	3.2	336.0	39.83160	-109.88473	103	2.9	357.7	39.84058	-109.92192
30	2.1	38.4	39.85266	-109.96478	67	7.1	19.1	39.83083	-109.88562	104	2.4	40.2	39.84095	-109.92294
31	1.7	23.9	39.85266	-109.96503	68	5.3	317.3	39.82994	-109.88623	105	2.0	23.8	39.84129	-109.92293
32	6.1	295.6	39.85205	-109.96543	69	2.4	331.4	39.82984	-109.88623	106	4.6	16.2	39.84155	-109.92307
33	1.4	231.4	39.85120	-109.96588	70	5.3	248.4	39.82920	-109.88601	107	1.4	297.9	39.84196	-109.92296
34	2.5	302.3	39.85074	-109.96549	71	1.6	296.9	39.82878	-109.88617	108	4.8	52.6	39.84206	-109.92286
35	9.0	37.1	39.85037	-109.96522	72	1.0	21.9	39.82856	-109.88646	109	5.3	35.7	39.84442	-109.92251
36	0.5	332.1	39.84995	-109.96624	73	11.4	189.5	39.82828	-109.88672	110	3.4	351.1	39.84535	-109.92306
37	0.6	60.0	39.84997	-109.96647	74	16.8	31.0	39.82808	-109.88710					

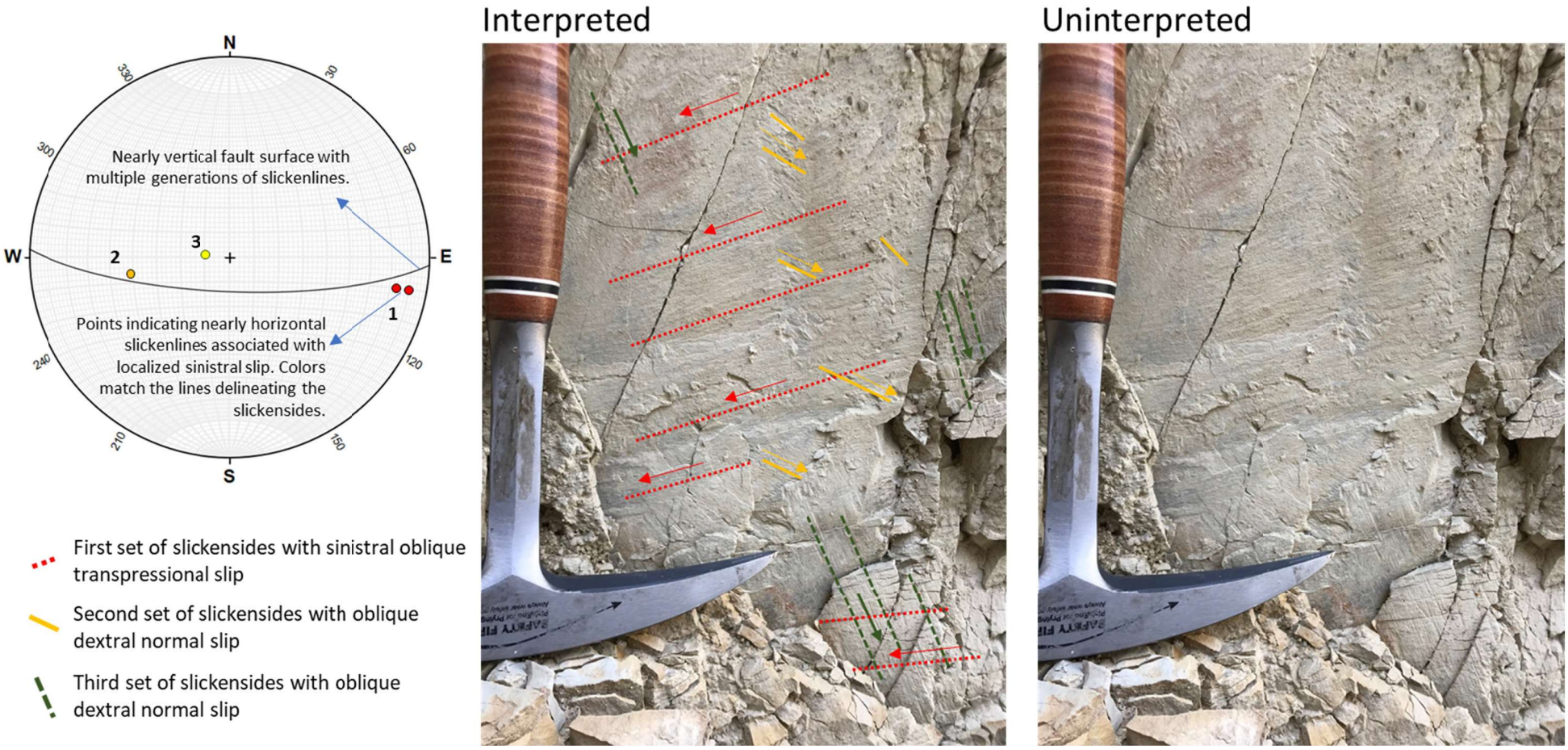

Figure 7. *Interpreted and uninterpreted photo of a fault surface on the S2 Sandstone in the central Sand Wash fault zone. This near vertical fault surface contains at least three generations of slickenlines, demonstrating how the sense of motion on the fault has changed over time. We interpret the set marked in red as being the oldest as subsequent slickenlines overprint them. These mostly strike-slip slickenlines were created when the fault was moving in a sinistral oblique direction under transpressional strain. Later, as the stress regime changed, the fault moved in an oblique dextral direction, then again in a more normal dextral sense of motion. These changing slip directions can be seen in the stereograph, with the fault surface represented as a great circle and the lines as points. The points are numbered in chronological order of slip (1 is oldest).*

Figure 8. *Plan view photo of the SWFZ as an example of methodology of the process of measuring fault length of discreet segments from drone-derived photogrammetry. Location shown in figure 4.*

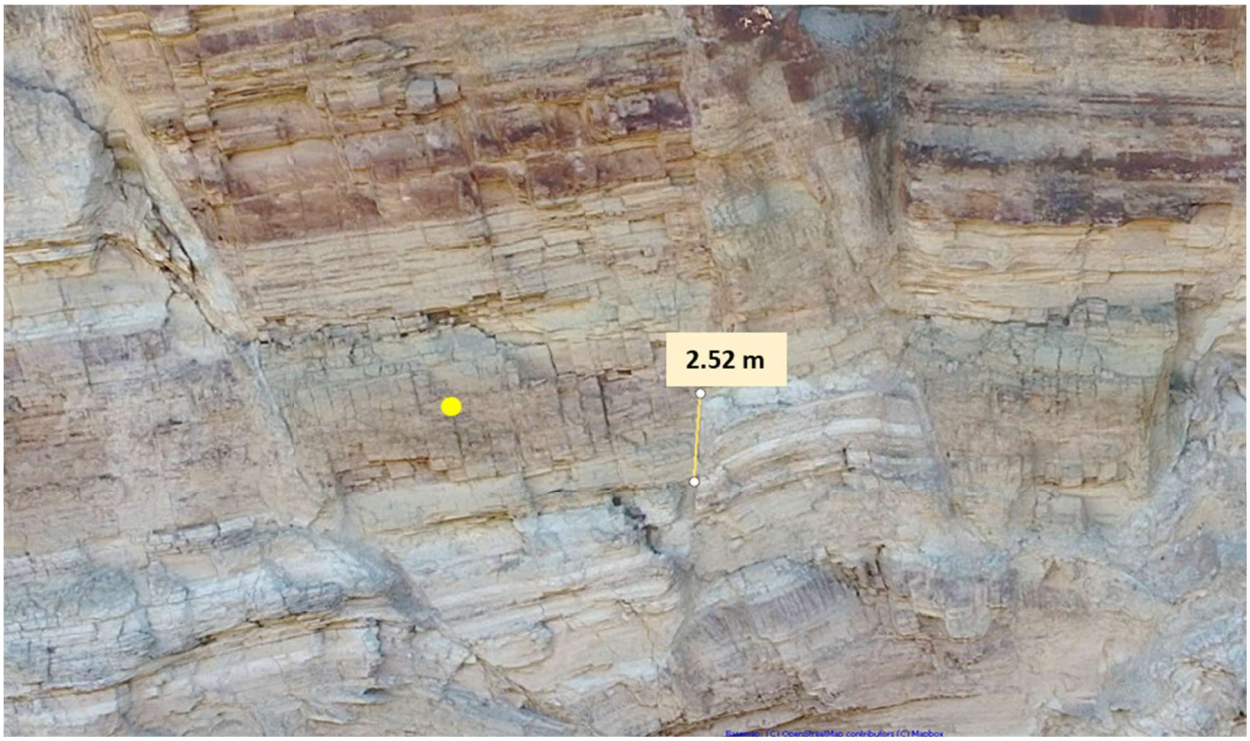

Figure 9. *Methodology of measuring fault displacements. GPS referenced photographs were taken of the cliff faces, which were then used to build large 3D models within Agisoft Metashape software. Looking east-south-east at the Nine Mile East photo pan. Note also the inclined joints sets (yellow dot) in the rotated fault block in the center of the image, indicating relative time between joint formation and block rotation.*

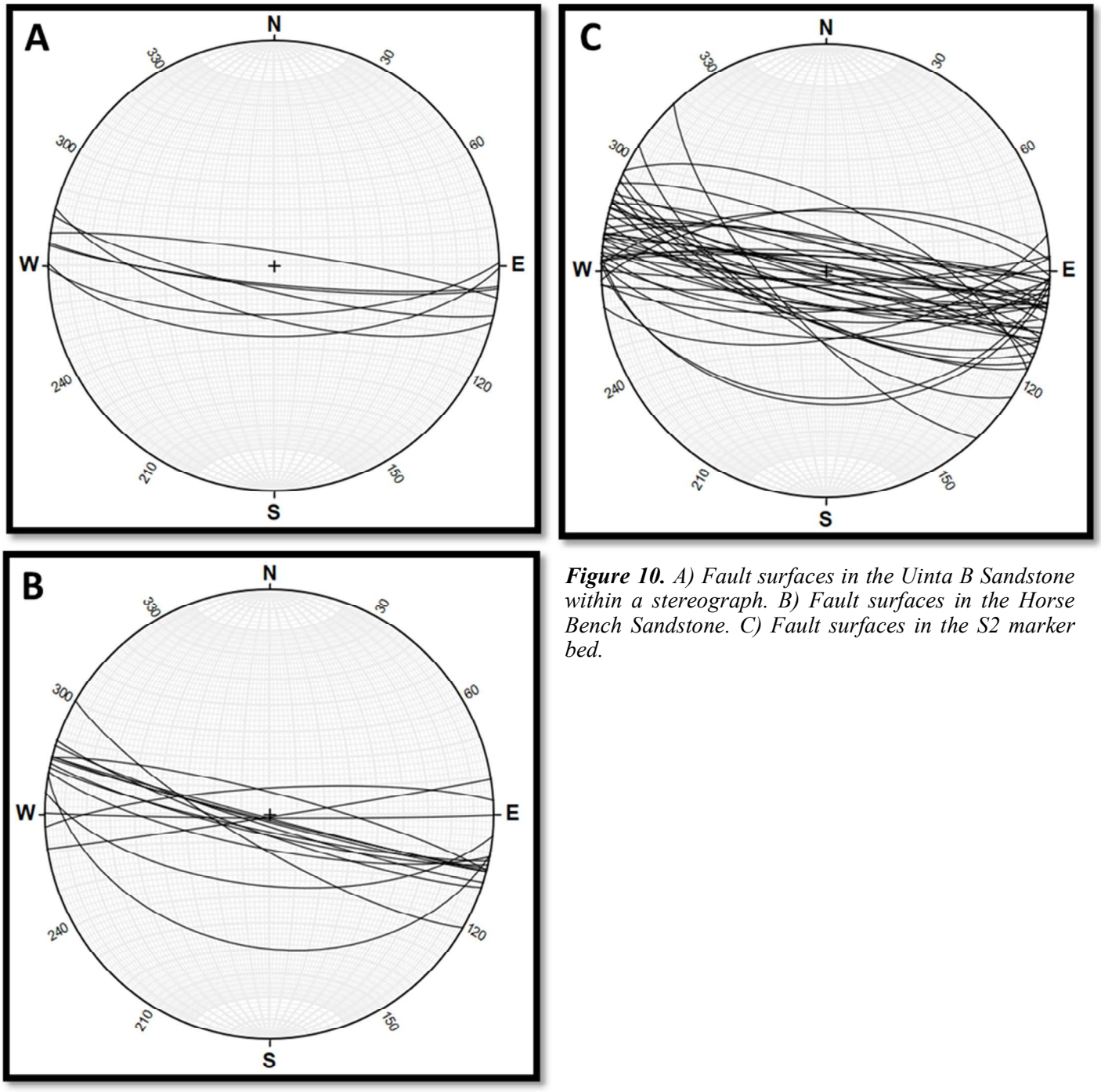

Figure 10. *A) Fault surfaces in the Uinta B Sandstone within a stereograph. B) Fault surfaces in the Horse Bench Sandstone. C) Fault surfaces in the S2 marker bed.*

stratigraphic intervals. Fracture sets within graben blocks were compared to joints and fractures outside of the grabens (table 5 and figures 12A and B). These fracture orientations were compared to the fault orientations from table 3 (figure 12C).

Fold axis data – Numerous folds were noted within the fault zone. These were classified by stratigraphic interval and fold type. The orientation of the axial plane of each fold was measured and compared by formation (table 6 and figures 13 A, B, C, and D).

Stratigraphic dips across the SWFZ – To better capture the larger scale deformation of the fault zone and a possible deformation mechanism, stratigraphic dips across from, within, and adjacent to the fault zones were taken and recorded (table 7). Figure 14 shows the distribution of stratigraphic orientation data from both within the SWFZ and adjacent dip slopes. Changes in the dip of both the S2 marker bed and Horse Bench sandstone, plus vertical offsets across the SWFZ were measured and drawn in profile (figure 15).

Geomechanical modeling - A simple geomechanical model was built to explore the differences between the sandstone and oil-shale beds. Unfortunately, the nearest well with wireline logs that could be used to build a complete geomechanical model with calculated elastic moduli of the sediments involved in this study (the Parachute Creek Member),

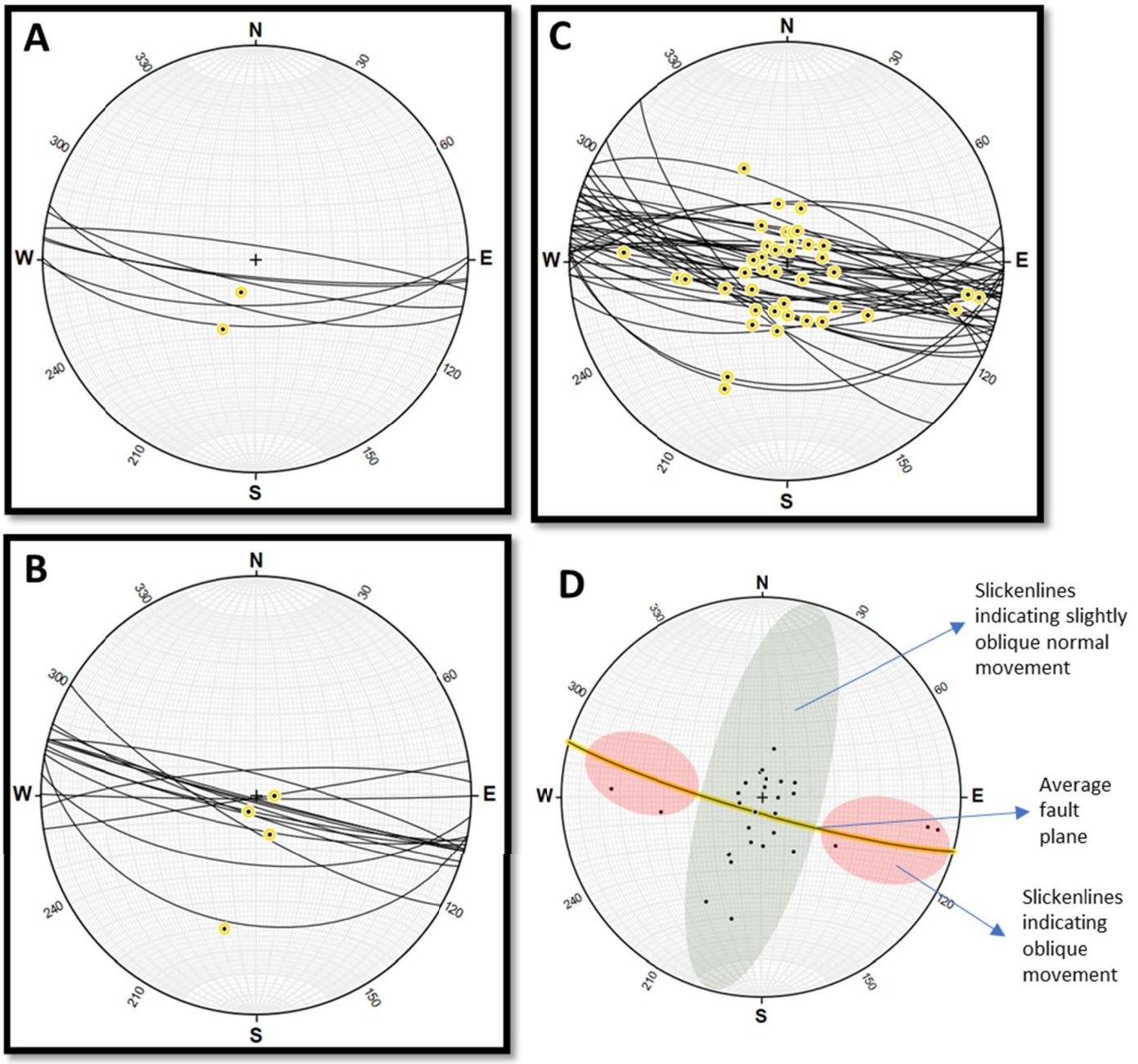

Figure 11. *A) Stereograph of slickenlines posted on fault surfaces from the Uinta Formation, member B. B) Slickenlines posted on fault surfaces from the Horse Bench Sandstone. C) Stereograph of slickenlines posted on fault surfaces from the S2 marker bed. D) Slickenlines from the S2 marker bed, with dip slip and oblique slip slickenlines indicated.*

such as dipole sonic logs, is about 32 kilometers north of the SWFZ, far enough that the stratigraphic units no longer correlate to those of the study area. Instead, we used more commonly available logs from the Pete's Wash Unit No. 14-24 (API No. 43-013-33202-0000), about 20 kilometers to the northwest from the center of the study area (figure 1). This well had good-quality gamma-ray, density, neutron, and sonic logs. Using the process described by Mews and others (2019), we calculated several log-based brittleness indices (LBI), plus total organic carbon (TOC) calibrated to the GRF as described in Brinkerhoff and Millard (2019). The LBI and TOC calculations are based on empirical relationships, with the LBI calculation outputting a 0% to 100% index and the TOC calculation outputting weight percent of organic carbon. The LBI index is easiest to understand when related to common materials, with an LBI of 0% having the brittleness of wet clay and an LBI of 100% the brittleness of glass (Mews and others, 2019).

Deep reflection seismic - Seismic reflection data publicly available from the U.S. Department of Energy was incorporated into this project. Fouch and others (1994b) evaluated wellbore and seismic data asso-

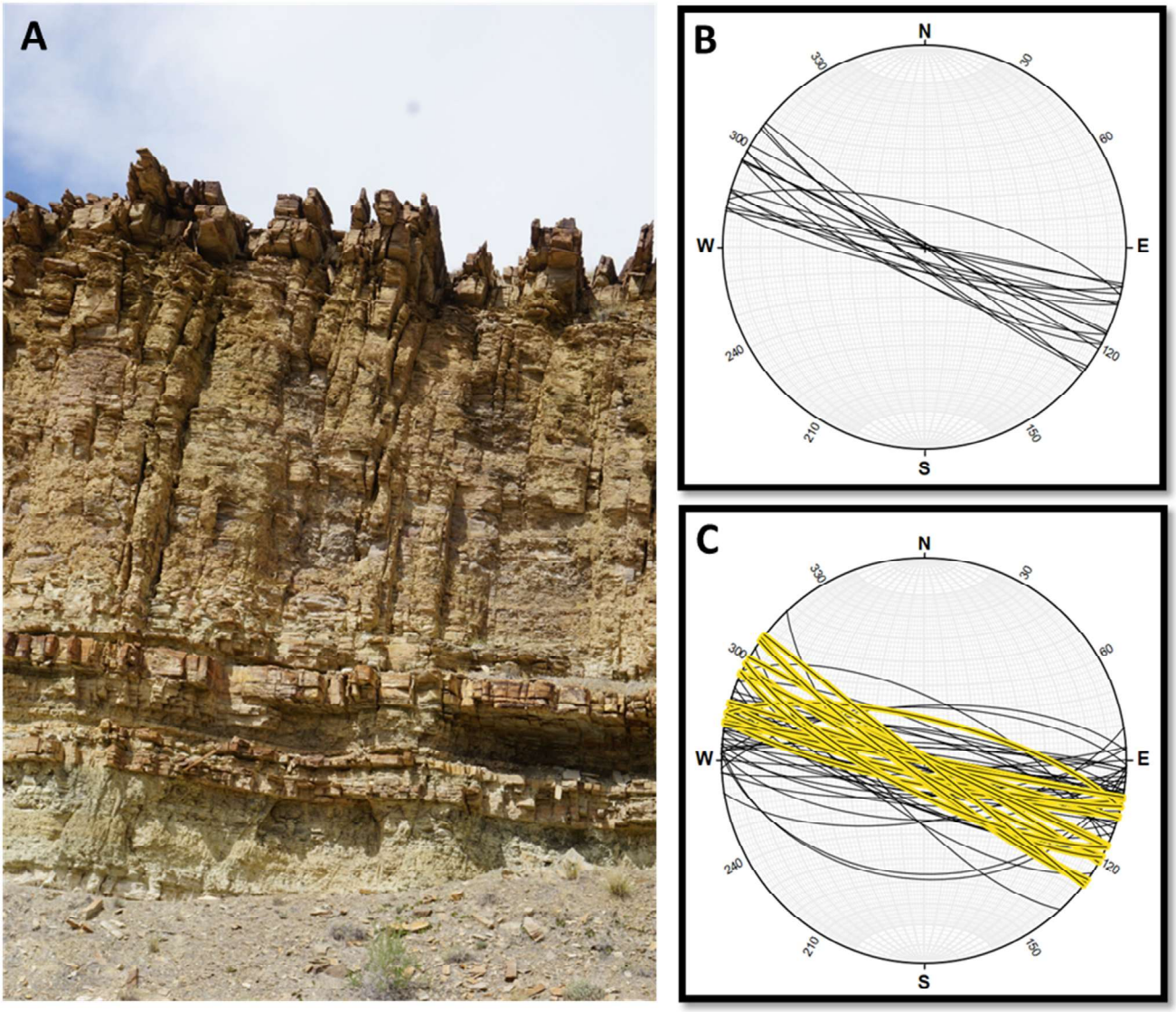

Figure 12. *A) Photo looking west-northwest of extensive jointing in the Horse Bench sandstone within the SWFZ. Note that the jointing is denser at the top of the Horse Bench in the cleanest sandstones and decreases in density downward. Cliff face is about 15 meters high. B) Stereograph of joint sets within the Sand Wash fault zone. C) Stereograph of joint sets (yellow) compared to fault surfaces (black). Note the about 5 clockwise rotation of average of the joint sets.*

ciated with the U.S. Naval Oil Shale Reserve 2, located on the east side of the Green River just south of the SWFZ and just to the southeast of the study area. Nine seismic lines were loaded into Geographix™ software and searched for deep structures as part of this study. Unfortunately, little under the SWFZ was interpretable as was on the far edge of the targeted surveys and fold count was low.

DATA AND RESULTS

Geometry and Kinematic Data

1. **Fault length and geometry data** – Altogether 222 subvertical fault segments were measured (table 1). The average segment length is 290 meters, but with a standard deviation of 285 meters, fault lengths are highly variable, particularly between different stratigraphic units. The stratigraphically highest units in the study area, the Uinta Formation, and the shales and siltstones in the upper parts of the Parachute Creek Member, have average fault segment lengths of 390 and 358 meters, respectively. Several segments in both units are over a kilometer in length. The S2 sandstone marker bed and Horse Bench Sandstone Bed have shorter average fault segments that are more tightly spaced within the fault zone.
2. **Fault displacement data** – The large number of measurements (93) capture the variation in vertical displacement magnitude within the fault zone. We focused on the S2 sandstone marker bed as it had the cleanest outcrops and most easily identifiable marker beds (table 2). For a

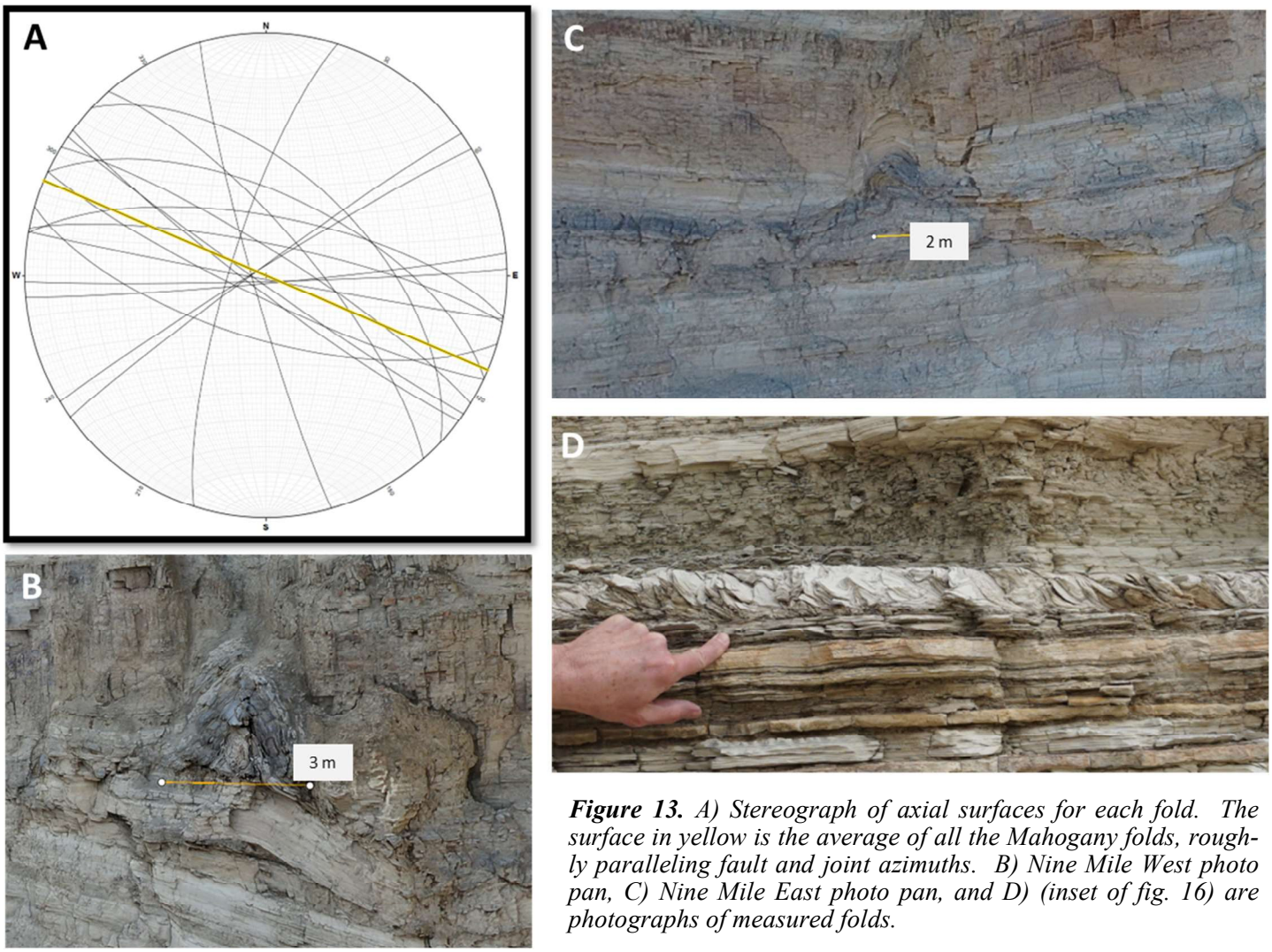

Figure 13. *A) Stereograph of axial surfaces for each fold. The surface in yellow is the average of all the Mahogany folds, roughly paralleling fault and joint azimuths. B) Nine Mile West photo pan, C) Nine Mile East photo pan, and D) (inset of fig. 16) are photographs of measured folds.*

wide fault zone, displacements are unexpectedly small with the largest offset measured being less than 5 meters and the average at only 1.34 meters. The fault segments are tightly spaced. For example, in a 164-meter outcrop we counted 41 significant fault segments. Within the core of the fault zone, fault segments are often spaced less than a meter apart.

3. **Magnitude of extension** – The cliff face in the Green River photo pan was clean enough to measure the total amount of horizontal extension at the top of the S2 sandstone marker bed (figure 3). The maximum horizontal extension is 33.5 meters. Errors in measurements could result in the total length of grabens and foundered blocks to be low, and the actual amount of horizontal extension may be several meters less than 33.5 meters. In any case, the total amount of horizontal extension is relatively low for a fault zone with the surface expression and length of the SWFZ (figure 2).
4. **Fault plane data** –Note that all three sandstone units exhibit the same fault azimuths, with most being sub-vertical but a few approaching 60° dip (tables 3 A, B, and C, plus associated stereographs). The individual faults parallel the azimuth of the larger fault zone, with some minor variance in the core of the zone related to stress shadowing between larger fault segments. Many of the better exposed fault surfaces were adjacent to weak gouges or shaley blocks. One large fault surface in the Uinta Formation was associated with a 1-meter-thick dike of calcite-cemented breccia (figure 16).
5. **Slickenline data** – Most slickenlines in this study indicate near dip-slip movement (tables 4 A, B, and C), with a smaller subset indicating strike slip associated with both right-lateral and left-lateral oblique displacement (figure 11D).
6. **Fracture data** – Sandstone beds within the study area are pervasively jointed (figure 12A). Dip angle and direction data (table 5) show that the existing joints closely parallel the fault system, with a slight, about 5°, clockwise rotation of the mean fault surface azimuth as compared to the mean joint azimuth (figures 12A and 12B). This may indicate a slight rotation of stresses between the onset of faulting with suffi-

cient lithification to allow jointing. Joint spacing within the S2 marker bed and Horse Bench Sandstone Bed vary between 0.45 and 1.5 meters, depending on bed thickness, cementation, and distance from the core of the fault zone. Joints do not penetrate the shaley beds above and below to the sandstones. Joints within some rotated fault blocks contained by grabens in the SWFZ show rotation, suggesting the relative timing between jointing and later graben development (figures 9 and 17A).

7. **Fold axis data** – Within the SWFZ, much of the differential shear between the deformed sandstones and the undeformed subjacent beds (figures 13B, C, and D) is accommodated by folding. Relatively large (up to 3 meters high) cylindrical, upright to slightly inclined and tight to isoclinal folds occur in the MOSZ immediately subjacent to the S2 sandstone marker bed, particularly in the richer oil-shale beds (figures 13B and C). Much smaller asymmetric, inclined, and transpositional folds appear in 5- to 20-centermeter-thick claystones near the base of the sandstones (figure 13D). Many axial surfaces are inclined and reveal the direction folds are verging using fold asymmetry relations. The fold data we collected is broken into two subparts, those found in the S2 marker bed and those from the MOSZ. The MOSZ dataset is more consistent, with the mean axial surface of folds largely paralleling the fault and joint azimuths that define the SWFZ. The S2 marker bed dataset is much more variable, likely reflecting the variable and complex motions these folds record (table 6). This geometric relationship is consistent with other data that reveal the close genetic relations between the SWFZ and folding (figure 13A).
8. **Features indicating syndepositional deformation** – Several observed folds and faults truncate abruptly against an overlying surface, indicating a cessation of major deformation and burial by younger sediments (figures 3, 18, and 19). Thickening of strata within fault blocks (figures 3 and 18A), ductile drag of footwall into faults indicating poorly lithified sediments (figures 3 and 18B), shortening of ductile (poorly lithified) sediments at the toe of foundered fault blocks (figure 18B), and small sag basins filled with heterolithic and chaotic strata (figure 19) all indicate that early motion on the fault zone occurred contemporaneous to lacustrine deposition. Keighley and others (2015) and Töro and Pratt (2015) presented evidence of significant and repeated syndepositional deformation of the MOSZ within the SWFZ, including slide blocks, debrites, and encased folds.
9. **Structural dip across the SWFZ** – In general, the steepest dips are found within the SWFZ where blocks have rotated as the fault zone experienced extension, having dips up to 25° (table 7). Dips outside of the fault zone were generally in the 2° to 6° range, having steeper dips north of the fault zone than south of it. This is best seen on dips projected from photogrammetry and surface profiles (figure 14). Dip slopes on the S2 sandstone marker bed show the greatest change across the SWFZ, with about 3° of change (figures 15A and B). This stratigraphic profile also showed about 3.5 meters vertical drop across the fault zone. The stratigraphically (180 meters) higher Horse Bench Sandstone Bed had a smaller dip change across the SWFZ, with only about 1.5° increase in dip.

INTERPRETATION

Relationship to Previous Work

Morgan and others (2002) and Morgan (2003) noted the complex internal structure of the SWFZ where it cuts the S2 marker bed, that individual fault displacements were small, and that displacement died out in the underlying MOSZ. Morgan and others (2002) also explored the Cedar Ridge fault zone (figures 5 and 20), which parallels the SWFZ 15 kilometers to the south. They noted that the core of this fault zone is also intensely brecciated. Furthermore, they speculated that the well-developed and thick gouge in the Cedar Ridge fault zone is likely caused by significant lateral movement associated with basement deformation. A geologic map of the Seep Ridge 30' × 60' quadrangle (Sprinkel, 2009) shows the Tabyago fault zone, an extension of the Cedar Ridge fault zone east of the Green River (sections 1 and 2, T. 14 S., R. 18 E., Salt Lake Base Line and Meridian; figure 20), deforming the Horse Bench Sandstone Bed, but not cutting the Parachute Creek shales below it, like what we find in the SWFZ. Fouch and others (1994b) evaluated several seismic profiles across the Tabyago fault zone. They interpreted basement-penetrating faults trending northwest-southeast, directly paralleling the SWFZ at depth, with a faulted dome at the Naturita Formation (formerly called the Dakota Formation) level, which they named the Tabyago dome. Both Stone (1977) and Eckels and others (2004) show the Seep Ridge fault zone as cutting basement with left-lateral movement about 2 kilometers south of and parallel to the SWFZ (figure

Figure 14. *Map of stratigraphic dips across the study area, with SWFZ traces marked in red.*

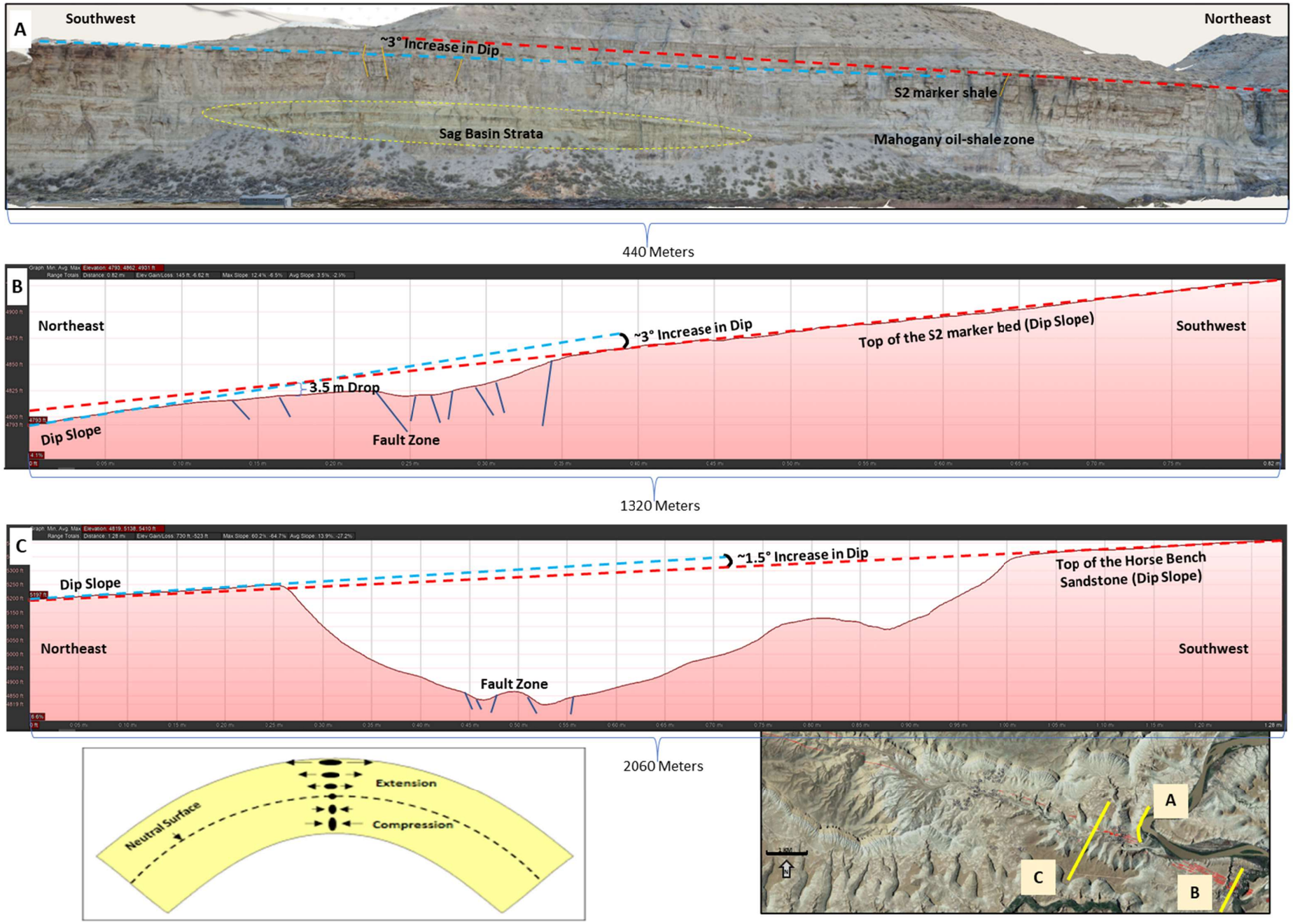

Figure 15. *Examples of the change in structural dip across the SWFZ and the broader folding that is the proximate cause the observed extensional faults. (A Photogrammetry of the cliff face at the mouth of Sand Wash Canyon. Note that stratigraphic dip projections from the northeast (red dashed line) are about 3° steeper than the projection from the southwest (blue dashed line). Also note the well exposed sag basin associated with the dip change. (B Surface elevation profile of the dip slope formed on the S2 marker bed, with dip projections drawn across the SWFZ. Note the vertical drop across the SWFZ and the 3° change in dips. (C Surface elevation profile on the Horse Bench profile, which is about 180 meters stratigraphically higher than the S2. The dip change is less pronounced, consistent with what would be expected that much above a neutral surface extension system.*

Figure 16. *Breccia dike (outlined in red) that intruded a fault in the Uinta Formation in the SWFZ. The fault contains slickenlines demonstrating dip slip, but the 2-meter-wide dike does not exhibit brittle deformational features, suggesting that the fault has not moved since intrusion. The neutral surface deformation model for the SWFZ has extension increasing upward, with a related drop in pressure. Dikes such as this fit this model. This breccia dike parallels and has similarities to the famous gilsonite veins 10 kilometers to the north. The dike likely intruded contemporaneously with the gilsonite veins in Oligocene during initial extension in the Uinta Basin.*

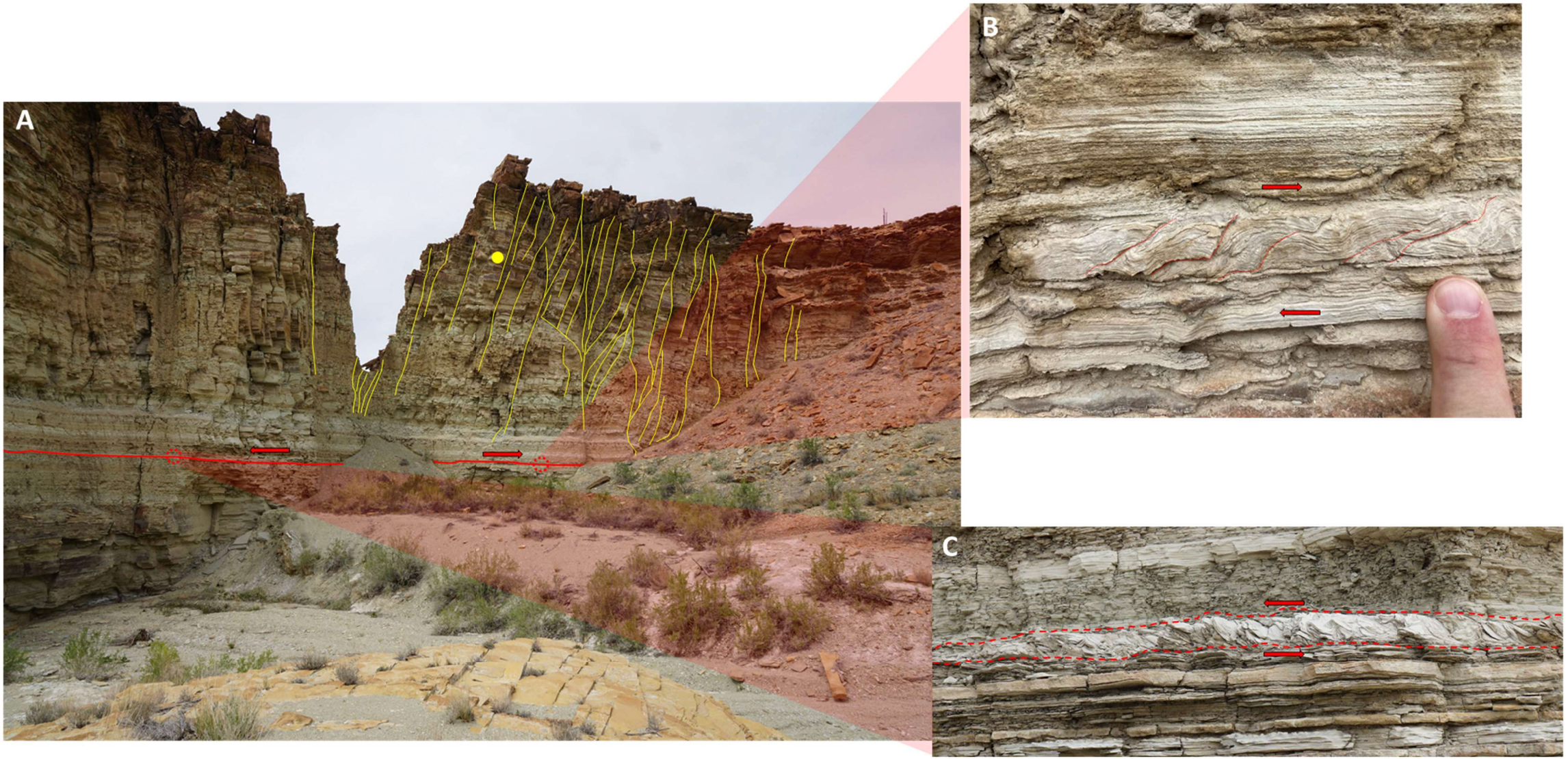

Figure 17. *A) Photo looking west-northwest at a décollement surface (in red) with micro-thrust duplex structures between the S2 marker bed (upper unit) and the Mahogany oil-shale zone, which varies across the study area, often with multiple horizons showing slip. Note also some of the sandstone blocks that experienced slip show inclined joints sets (yellow dot), indicating joint formation occurred before block rotation. Stratigraphic dip on the Mahogany oil-shale zone also changes from nearly horizontal on the left side of the photograph to over 10° on the right. B) and C) detail of thrust duplex systems with imbrication of thrust sheets between roof and floor thrusts.*

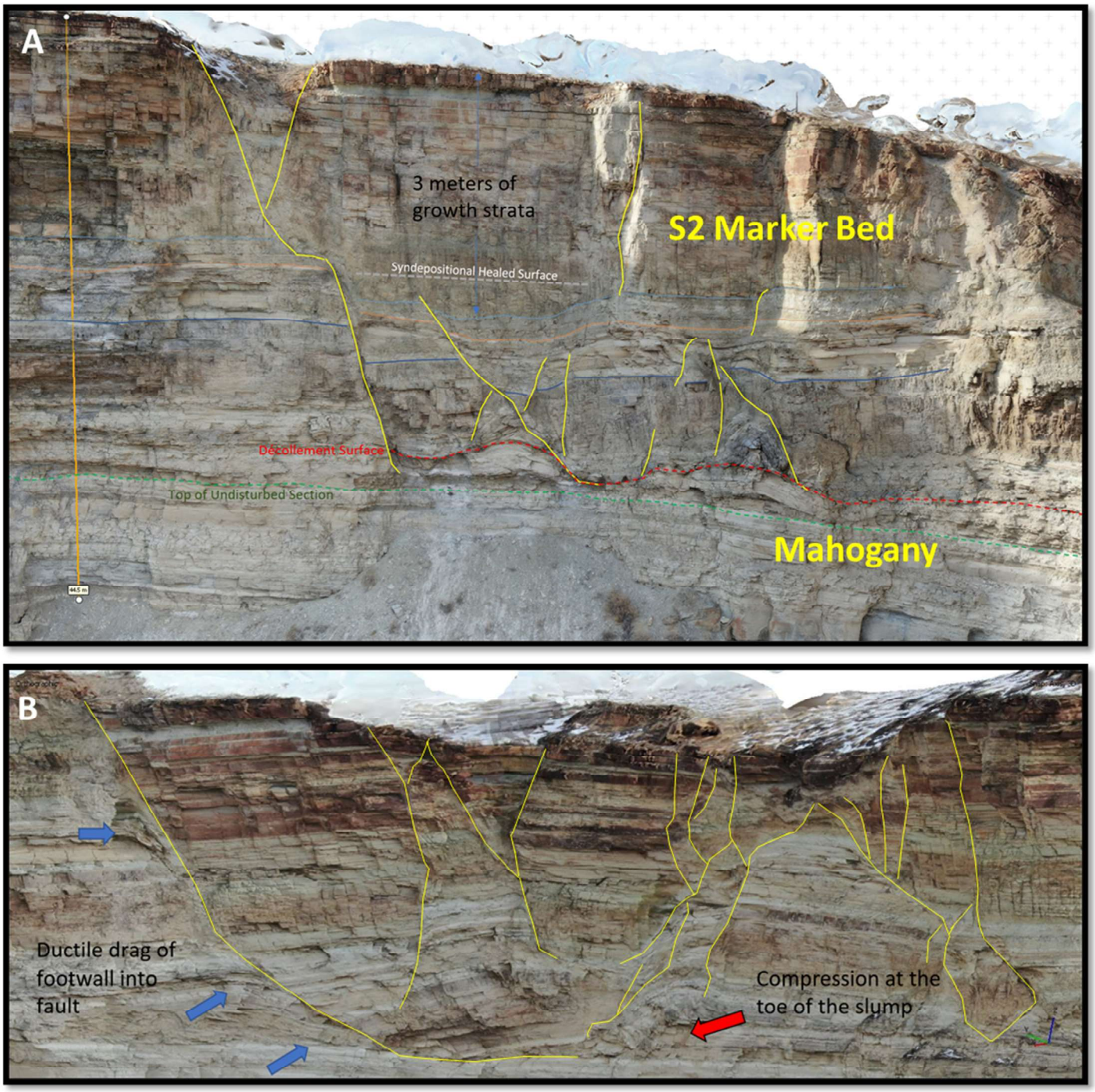

Figure 18. *Composite images of SWFZ showing evidence of syndepositional fault movement (faults outlined in yellow). A) Cliff face on the west side of Nine Mile Creek, looking west-northwest. It has a well-developed decollement surface under a series of fault blocks that were also deformed, likely because they were newly deposited and poorly lithified while being deformed. Syndepositional healed surfaces and growth strata also indicate syndepositional movement on this fault. B) Cliff face on the east side of Nine Mile Creek, looking east-southeast, with large, rotated blocks with fault drag and shortening on the footwall, indicating poor lithification and deformation early after burial.*

20). Stone (1977) and Eckels and others (2004) also directly connect the Cedar Ridge fault zone with the Garmesa fault zone which also has sinistral movement based on seismic data, fault surface analysis, and en echelon folds. These workers interpret these faults as being associated with the Uncompahgre uplift because the larger faults connect directly with that uplift to the southeast of our study area, and smaller fault systems directly parallel the larger systems (figures 5 and 20). The SWFZ is immediately parallel to the Seep Ridge fault zone and its eastern terminus is only about 5 kilometers to the northeast of that fault. These two faults share many characteristics with the Cedar Ridge fault zone in outcrop, again suggesting a similar genesis. However, Morgan and others (2002) classified the SWFZ as a non-basement-

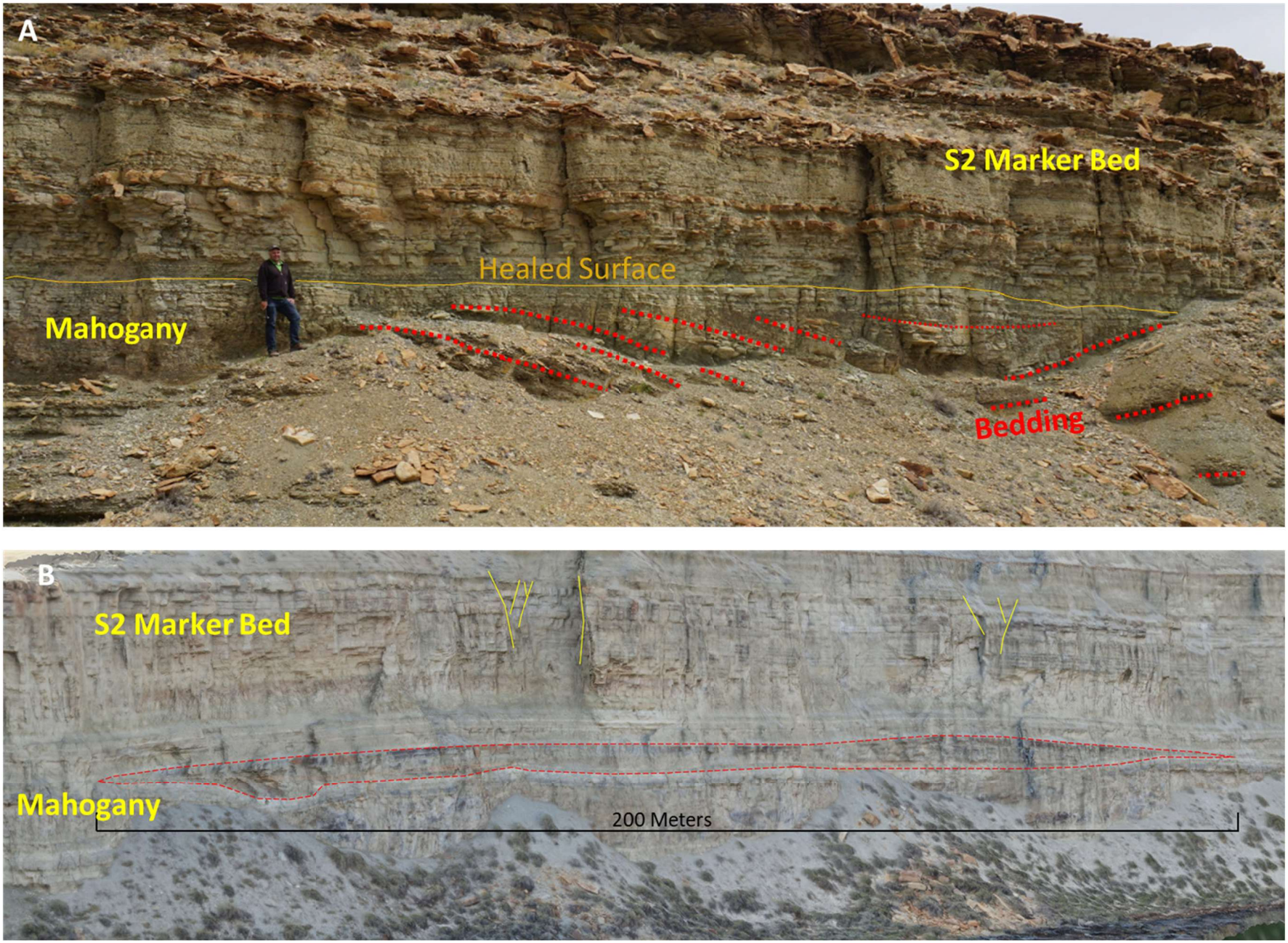

Figure 19. *A) Photograph, looking east-southeast, of small sag basin near the top of the Mahogany zone. The sag basin is filled with a heterolithic mixture of mudstones and siltstones capped by an underformed "healed surface." Two-meter-high geologist for scale. B) A larger sag basin found on a cliff face of the Mahogany zone near the Green River. It also is filled with a heterolithic mixture but is much larger in scale.*

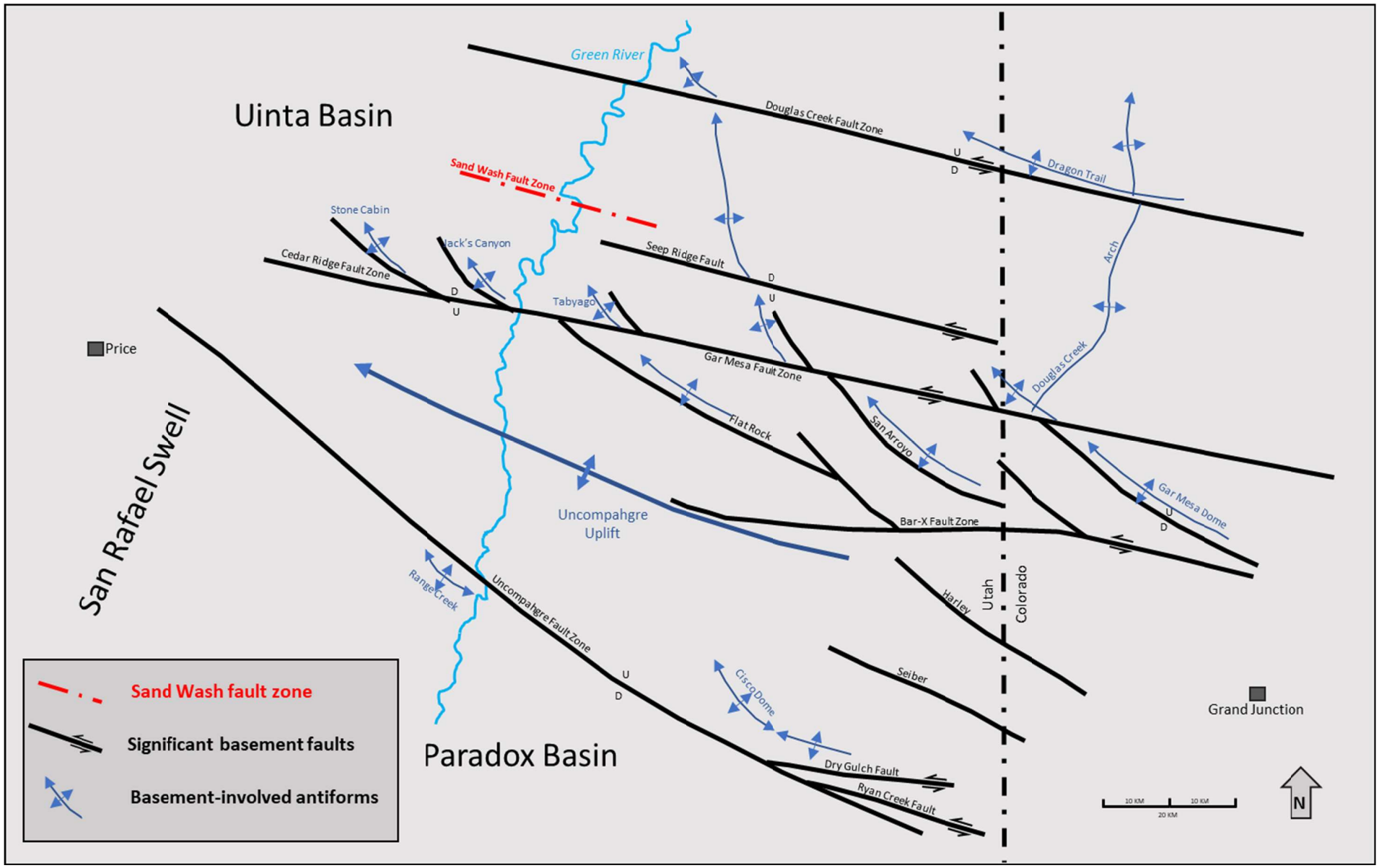

Figure 20. *Map of significant basement faults and antiforms related to the Uncompahgre uplift. Many of these faults are features that are only partially expressed in the overlying sedimentary cover. Note the consistent trend of the structures and their relationship with the SWFZ. Modified from Stone (1977), and Eckels and others (2004).*

involved fault zone, related to "hinge zone" flexures based on the observation that faults cutting the S2 sandstone marker bed sole out in the MOSZ.

Review of Paleogene Tectonic Regime in the Uinta Basin

The Late Cretaceous-Eocene Laramide contraction (Mederos and others, 2005) lifted the Uinta, Uncompahgre, San Rafael, and Douglas Creek blocks (figure 5). These blocks bound the Uinta Basin (Johnson, 1985; Dickinson and others, 1986) and contain faults and other structures with Laramide dextral shearing (Sprinkel, 2018). The Uncompahgre uplift and Douglas Creek arch show concurrent sinistral movement (Bader, 2009; Stone, 1977). The Uncompahgre block/uplift is particularly important in this discussion because it plunges northwest beneath the Uinta Basin, influencing structural trends near the SWFZ (figure 5). The SWFZ and other faults in the area parallel the trend of Uncompahgre uplift fold axes that plunge beneath basin deposits. The larger SWFZ antiformal structure is interpreted to have formed during sinistral shear in the Laramide in concert with the movement on the underlying Uncompahgre block (Bader, 2009); thus, indicating that SWFZ is likely related to deeper oblique-slip faulting (reverse-sinistral P-shear) in the Laramide.

The large fault zones within the study area, such as the Gar Mesa, Cedar Ridge, and Seep Ridge fault zones have been shown to be basement-rooted faults (figure 20). They are interpreted to show evidence of sinistral movement based on; (1) seismic data, (2) outcrop exposures on the Douglas Creek arch and Uncompahgre uplift, (3) observations of sinistral-slip related folding, and (4) their similarities to analogous faults that either have basement exposure or have data such as seismic that so demonstrates (Stone, 1977; Fouch et al., 1994a; Eckels et al., 2004; Bader, 2009). Marshak and others (2003) contend that the many parallel traces in the sedimentary cover of these basement-penetrating strike-slip faults occur because the shallow (1 to 2 kilometers thick) sediments are too weak to maintain a single point of breakage. Instead, deformation is distributed through multiple points of shear across the developing fault zone. Deeper, stronger rocks tend to localize displacement along a few or only one fault strand as the rocks have the strength to concentrate shear.

With the close of the Laramide orogeny in the Oligocene, compressional stresses in the Uinta Basin relaxed (Verbeek and Grout, 1993; Wawrzyniec and others, 2002). The many gilsonite dikes in the Uinta Basin, which roughly parallel the SWFZ, are believed to have been injected along preexisting joints in the early stages of post-Laramide regional tectonic extension (Verbeek and Grout, 1993; Boden and Tripp, 2012). Bader (2009) shows evidence of dextral slip in early post-Laramide time within fault zones on the Douglas Creek arch and west into the Uinta Basin, including our study area. This is likely related to northwestern translation of the Colorado Plateau and the opening of the Rio Grande Rift (Grout and Verbeek, 1998; Wawrzyniec and others, 2002; Bader, 2008). Finally, this all suggests that Laramide fault zones across the Uinta Basin, including the SWFZ, Cedar Ridge and Duchesne fault zones, were reactivated during Neogene extension (Sprinkel, 2018; Brinkerhoff and Sprinkel, 2021; Howe and Klinger, 2021) with most forming small grabens. These extensional features are also exhibited on major faults as well, including the Uinta uplift boundary fault zone (Sprinkel, 2018), the Garmesa and Douglas Creek fault zones (Johnson and Finn, 1986; Bader, 2009), and the Duchesne fault zone (Brinkerhoff and Sprinkel, 2021).

DISCUSSION

As described from the preceding datasets, the Sand Wash fault system varies along its length and within its exposed stratigraphic units. In the S2 sandstone marker bed, the stratigraphically lowest sandstone body exposed within the fault zone, the fault consists of a thick (up to 10 meters) core of fractured gouge and breccia (figure 21). Outside the gouge zone are closely spaced synthetic and antithetic faults. Individual faults gradually become further separated, until the outer part of the fault zone becomes closely spaced joint sets that parallel the fault zone (figure 12A). Fault displacements in the S2 marker bed sole out in the underlying oil shales of the MOSZ. However, individual faults of the SWFZ that cut the Horse Bench Sandstone Bed and sandstone beds of the Uinta Formation (Uinta B member) (figure 6) also sole out into the underlying Parachute Creek Member oil shales. The faults rapidly lose vertical throw downwards, dying out completely in tightly spaced folds in the upper 10 meters of the underlying lacustrine oil shales (figures 3, 17, 18, and 21). Within 5 meters below, the oil shales are relatively undeformed (figures 17A and 18A). Sandstones within lacustrine oil shales in the overlying section, such as the Horse Bench Sandstone, exhibit a similar deformational fabric. We believe the mechanism for the vast difference in deformation between the brittle sandstones and the oil shales lies in the large difference in shear strength between these units.

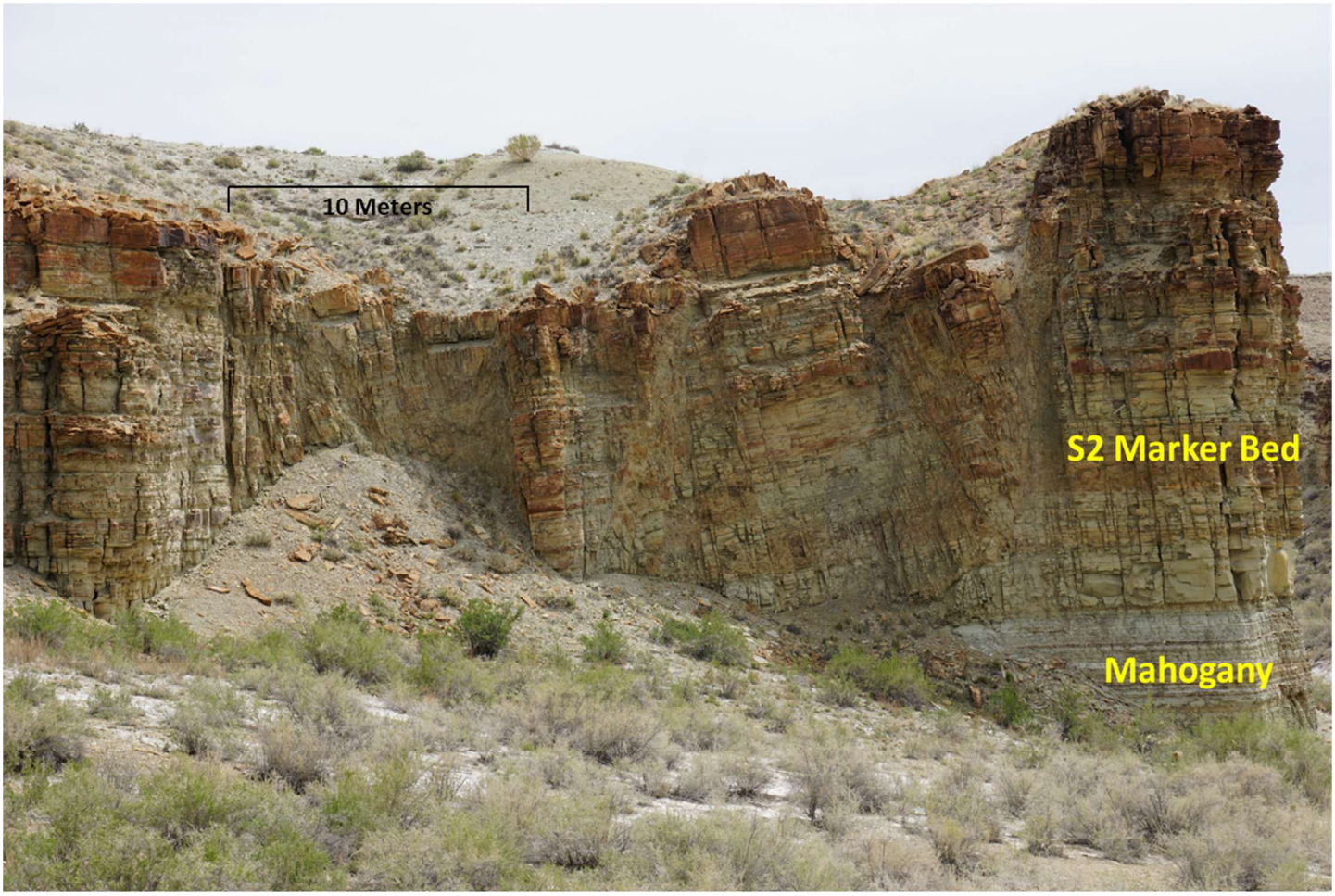

Figure 21. *Photograph of the SWFZ in the S2 marker bed. Note the rotation of blocks and joints inside the fault zone. Also note the well-developed damage zone and high density of fractures in the sandstone, particularly as compared to the underlying shale.*

Syndepositional Deformation

The SWFZ appears to have been active as lacustrine sediments accumulated in Eocene time. The most impressive syndepositional structures occur in the S2 sandstone marker bed and include fault arrays that terminate upward at a healed surface, indicating repeated rupturing separated by intervals of inactivity (figure 18A). These faults are also associated with foundering blocks that exhibit growth strata, ductile footwall drag, changes in bed thickness, slumps, contractional structures, and compression of sediments (figures 3, 18, and 19). These features appear in sandstone beds without associated fracturing, indicating that these beds had not yet lithified.

The MOSZ is also affected by the syndepositional movement on the SWFZ. Keighley and others (2015) documented extensively disturbed strata. Overlying healed surfaces within the MOSZ directly underlie the faulted S2 marker bed. The Mahogany bed in the SWFZ is most often present as; (1) discontinuous tilted rafts, (2) stratigraphically repeated zones (up to 10 meters thick) of extensively folded and deformed beds of muddy sandstone, and (3) debrites and diamictites within specific outcrops along Sand Wash Canyon. Keighley and others (2015) interpreted the deformation as being caused by liquefaction and downslope gravitational movement via slumping. While invoking a possible large, basin-wide earthquake, they did not believe that movement on the SWFZ was responsible, as no faults completely cut the MOSZ. The photo pans from this study show relatively small sag basins (figure 19 within the MOSZ, likely related to movement on the SWFZ. These features are like the slightly older sag basins within the Long Point Bed found in the Duchesne fault zone documented from subsurface data (Brinkerhoff and Sprinkel, 2021). Since the sag basins and large-scale disruptions of the MOSZ underlie SWFZ deformation in the S2 sandstone marker bed, we believe that they are related to syndepositional fault movement. The newly created subsiding basins accommodated accumulation of the disrupted Mahogany beds. In addition, the slope and energy related to fault movements could mobilize the debrites and diamictites. Small folds and minor rafts of oil shale have been found in

the MOSZ in several places across the basin (Bradley, 1931; Cashion, 1967; Grabowski and Peaver, 1985; Keighley and others, 2015; Töro and Pratt, 2015) but there is nothing on the scale of the deformation of the MOSZ along the SWFZ. This level of mass movement and folding appears to be localized near the SWFZ.

Like the underlying MOSZ, the S2 marker bed, Horse Bench Sandstone Bed, and Uinta Formation sandstone beds have prominent and pervasive soft-sediment deformation (SSD) in the SWFZ. SSD in Green River sandstone beds has been noted by many previous workers (Bradley, 1931; Remy, 1992; Birgenheier and Vanden Berg, 2011; Töro and Pratt, 2015; Brinkerhoff, 2019), many noting the large and very impressive SSD structures found across the Uinta Basin. The deformation along the SWFZ is noteworthy due to its prevalence. Almost every sandstone unit with 10- to 30-centimeter-thick beds has widespread flame, and ball and pillow structures, features expected if the deposits were subjected to repeated shaking within a fault zone. The difference in syndepositional deformation between the MOSZ (slumping, sag basins, debrites) and the sandstones (flame structures, ball and pillow structures, slumping) appears to be related to different rheological responses to the same tectonic stresses experienced by sediments accumulating on the SWFZ.

Local SSD and slumping in GRF sediments are common across the Uinta Basin. However, stratigraphically repeated features, which indicate syndepositional folding and shaking along a narrow zone 1 kilometer wide and 34 kilometer long, indicate that the causative stress is likely associated with movement on a deep-seated fault. Strain on this fault was partially uncoupled at the surface, with oil shales responding with large, yet shallow slumps and flows and small-scale subsidence (the sag basins). The sandstones experienced steeper block movement along small faults that were then buried by later sediments, creating fault segments that end at healed surfaces.

THE RELATION OF THE SWFZ TO ADJACENT FAULT SYSTEMS

In our interpretation, the Cedar Ridge and Seep Ridge fault zones, and other nearby fault systems that parallel the SWFZ, are structurally related to one another and to the mobile Uncompahgre block (figure 20). Stone (1977) and Bader (2009) document Eocene movement on the large fault systems within the study area, contemporaneous with the syndepositional deformation observed in the SWFZ. Deformation continued within the SWFZ, as demonstrated by the jointing that occurred in the sandstones after lithification and the continued fault movement in younger, overlying strata.

The well-developed gouge and wide damage zone of the SWFZ (figure 21) in the sandstone units suggest repeated movements. By plotting the strike of the SWFZ's well-developed joint system (figure 12B) and individual fault surfaces (figure 12C), we can surmise that the SWFZ was responding to the same stress field created by the Uncompahgre uplift as the Cedar Ridge, Gar Mesa, Seep Ridge, and other parallel fault zones within the study area. The parallel fault systems south of the SWFZ have significant strike-slip offsets (Stone, 1977; Bader, 2009).

Sense of Movement on the SWFZ

Within the SWFZ our observations mostly indicate normal movement. The majority of slickenlines indicate dip slip (figures 11A, B, and C), and the fracture sets, both joints and conjugate fractures, indicate that the maximum stress component (sigma 1) was vertical. Although sigma 2 was parallel to the fault zone, it was not sufficient to force transpressional movement. Significant strike-slip movement does not appear to have occurred within the studied sediments at the current ground surface on the SWFZ after lithification.

Of the 50 slickenline measurements, the majority show simple dip slip, or slightly oblique dip slip. This may be expected as the latest movements on the fault zone were extensional. We did find a few surfaces with multiple generations of slickenlines (figure 7), with the latest, most prominent being dip slip, but older slickenlines may show oblique-to-strike-slip movement, possibly from the rotation of blocks during extension. However, additional supporting data suggesting strike slip, such as Riedel shears or offset pinpoints, were not found in the study area. While deep strike slip could have occurred before lithification, we believe that the stress field was largely normal after lithification.

Folds

Folding of clay-rich rocks is prominent in the SWFZ, mostly in the lower parts of the S2 sandstone marker bed and the upper parts of the MOSZ (figures 13B, C, and D). Stereographs of fold hinge lines and axial planes (figure 13A) show that the folds formed in two groups, (1) folds with axes parallel to the SWFZ, which are very common in the MOSZ, and (2) folds with variable axes, which are more often

found in the S2 sandstone marker bed. We interpret these folds as accommodating the relative movement between the overlying sandstone bodies and the underlying, largely undeformed, oil shales. Folding may have accommodated syndepositional oblique- and strike-slip motion. The parallel folds likely accommodated the extensional motion above a neutral surface of the larger fold across the SWFZ (figures 15 and 16). Décollement surfaces are also present, where the overlying zone simply moved over the lower unit with little internal deformation of the overlying or underlying blocks (figures 13D and 17).

Geomechanical Stratigraphy

Geomechanical modeling shows why the sandstone beds were so pervasively shattered and deformed whereas the oil shale beds were left mostly undeformed (figure 22). The S2 marker bed calculated very low TOC and LBI values in the 60% to 92% range, averaging 83%. The MOSZ had much higher organic content, as would be expected, with TOC values in the 6% range, and much lower LBI's, in the 10% to 70% range, averaging 45% (figure 22). Comparing different LBI and TOC values in the MOSZ with that of the overlying S2 marker bed suggests that

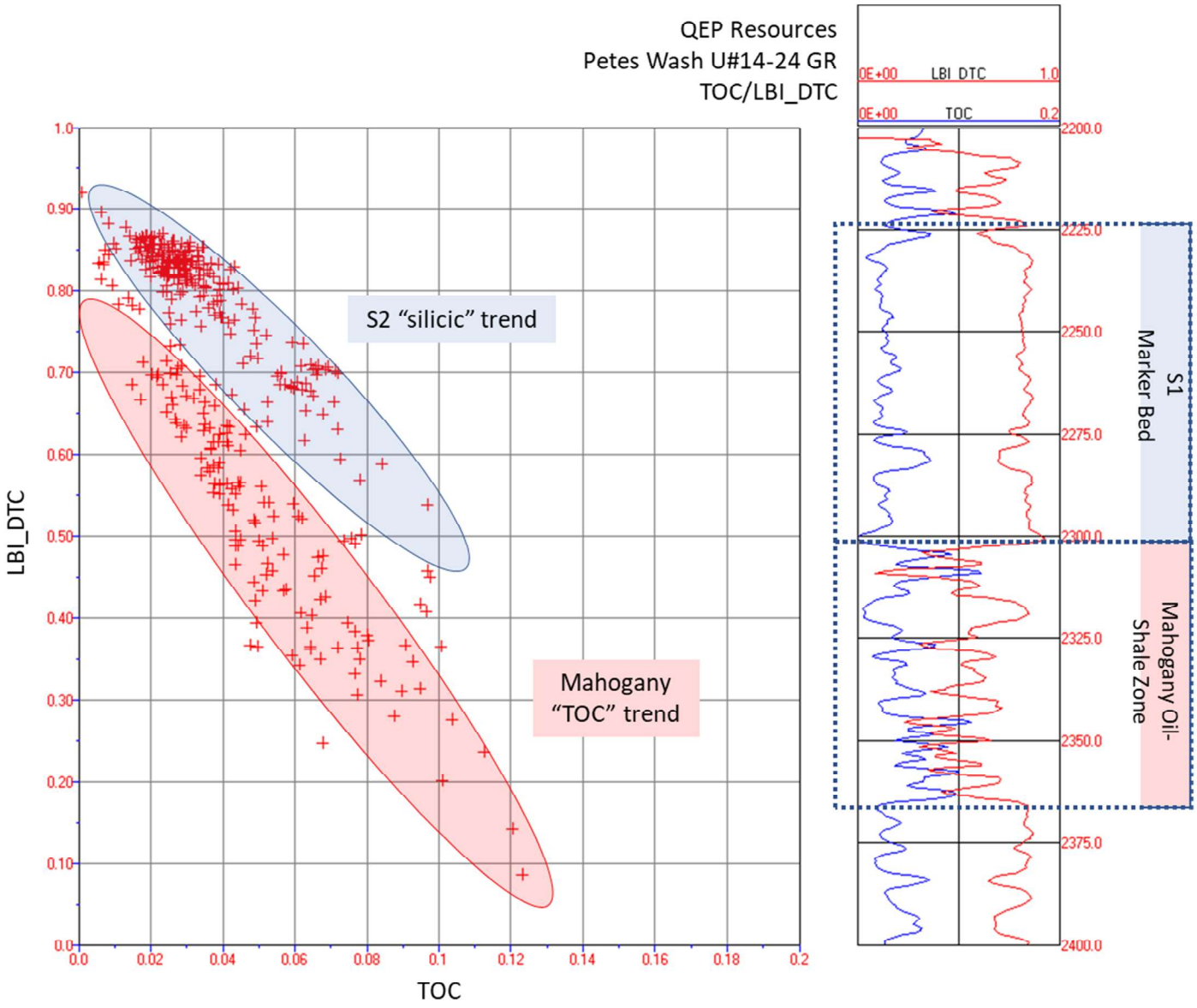

Figure 22. *Cross-plot and wireline log segment of the S2 marker bed (in light blue) and the Mahogany zone (in pink). The cross-plot compares a log-based brittleness index with a log-based TOC percentage. Note that in general the S2 marker bed is more brittle than the Mahogany oil-shale zone at any given TOC because it lacked the granular matix to accommodate TOC without losing strength. Additional TOC caused the Mahogany zone to respond ductilely. Brittleness indices such as this demonstrate how the mechanical properties of each unit influence what is deformed by varying degrees of distributed strain.*

these units should react to tectonic stresses very differently. TOC and LBI trend oppositely, i.e., higher TOC values correlate tightly with lower LBI values. This correlation is tied to mineralogy (figure 22). The higher quartz percentage in the S2 sandstone forms a distinct and shallower trend than the clay and carbonate rich MOSZ. The relationship of higher ductility in Mahogany beds with greater TOC volumes has been noted previously (Birgenheier and Vanden Berg, 2011; Bader, 2009). During early burial and lithification, extensional stresses were applied on the entire section because of deeper vertical movement and folding across the SWFZ. The extreme ductility of the Parachute Creek oil-shale beds, and particularly the MOSZ, distributed this strain more evenly, without a single point of rupture, such as a fault. The joint sets that are so prominent in the brittle sandstone units could not propagate into the ductile oil shales. Fault movement was simply absorbed by minor folding of immediately adjacent units and layer-parallel slippage, creating the décollements observed in outcrop.

CONCLUSIONS

The SWFZ developed during the Laramide orogeny as the result of extension above the neutral surface of a large-scale fold. Across the SWFZ, average structural dip increases by about 3°, which is coupled with a 3.5-meter vertical drop (figure 15B). The dip change is likely related to the same type of basement-involved faulting observed in seismic at the Tabyago fold (Fouch and others, 1994b). The SWFZ formed because of folding beneath it versus connection with some regional décollement. Evidence for this is decrease in displacement downward and the parallelism of fold axes to the fault plane (figure 13A).

The SWFZ is an instructive structural laboratory for documenting various deformation mechanisms that operated simultaneously based on variations in the mechanical stratigraphy. The immense importance of the geomechanical qualities of rocks in the propagation of faults and fractures can be easily observed. Strain partitioning is recognized in brittle failure of sandstones directly overlying ductile folding and small décollements in oil shales, with the best examples being the S2 sandstone marker bed and the MOSZ. Well-developed fault gouges are surrounded by synthetic and antithetic faults, both easily accessible and interpretable. One can also quite easily discern the distinct deformation styles of faulting in pre- and post-lithification sandstones, and how sedimentary systems are influenced by active fault systems. It is also instructive to compare the SWFZ with the parallel fault systems farther south, such as the Cedar Ridge fault zone. Like the SWFZ, these faults were also formed by movement related to the Uncompahgre uplift. They differ in that the stratigraphy exposed farther south is older and deeper than that at the SWFZ.

By combining our interpretation of the SWFZ with the regional structural history, we can build a deformation history for the fault zone (figure 23).

Eocene – Syndepositional

This developing fault zone shows syndepositional activity in Eocene time, during the deposition of the MOSZ, resulting in small sag basins and rafts of oil-shale beds, debrites, and irregular inclined beds (figure 23A). During the deposition of the overlying S2 sandstone marker bed, slumping, foundered blocks, growth strata, and well-developed flame structures were induced into the sediments shortly after deposition by extension and repeated shaking on the developing SWFZ (figure 23B).

Eocene – Post Lithification

After lithification, stress on the SWFZ formed intense northwest-southeast-trending joint sets in the brittle sandstones (figure 23C). With greater stress, joint sets began to coalesce into small faults in a zone about a kilometer wide. This fault zone continued to develop through late Laramide time, with the oldest (and presumably first lithified) sandstone exposed in the study area, the S2, experiencing the greatest amount of deformation, with progressively less deformation in the sandstone units moving up section. The ductile oil-shale beds were largely unaffected after lithification, while the sandstones were deformed near the shale beds, creating folds and décollements perpendicular to the trend of the fault zone.

Oligocene

Stress regime changes at the end of the Laramide orogeny caused transtensional deformation in the Uinta Basin as it moved to the northwest with the rotation of the Colorado Plateau. With the cessation of Laramide stresses, overpressured fluids intruded existing fractures, forming gilsonite veins to the northeast of the SWFZ and paralleling it, and the breccia dikes (figure 16) within the SWFZ. Many of the faults that had moved in Laramide time were reactivated and underwent dextral slip. While faults in the SWFZ likely did not significantly move, the change in the stress field likely did cause additional fracturing and enlarging of the SWFZ.

Miocene

With major Basin and Range extension in western and central Utah beginning in Miocene time, the Uinta Basin extended further, causing

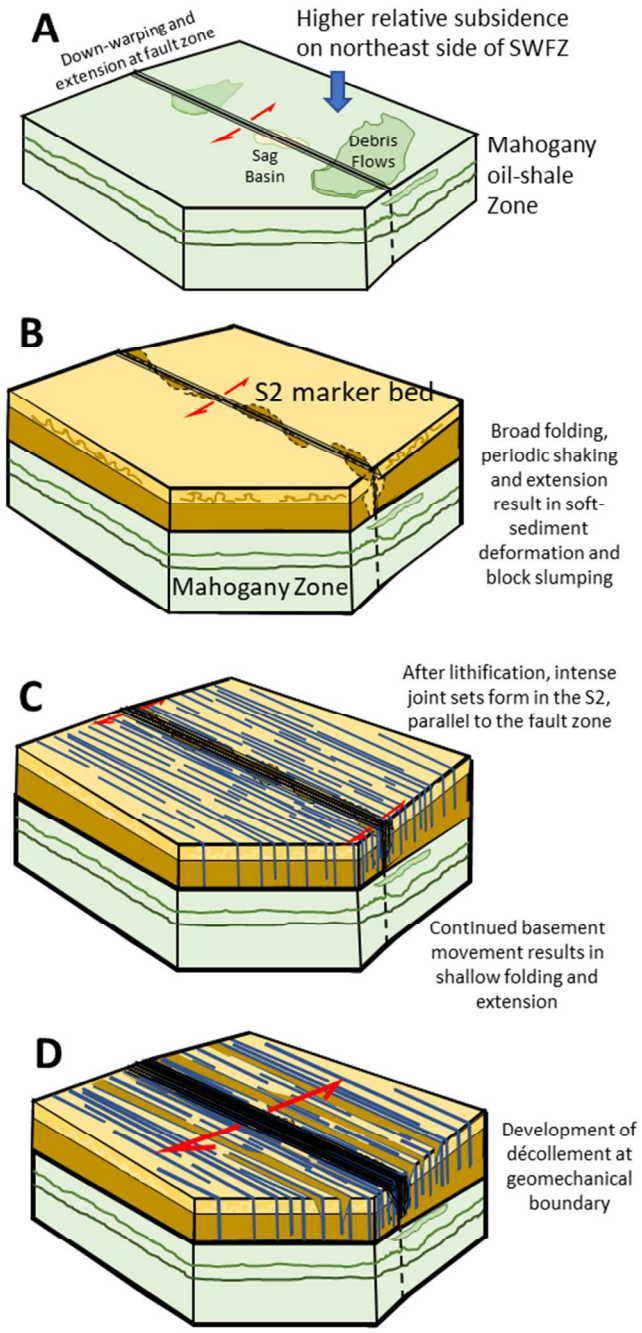

Figure 23. *Model of the structural development of the SWFZ. A) During the late Eocene at Mahogany time, surface folding connected to movement on the deep Uncompahgre-related folds results recurrent shaking, minor extension, and basin-ward down warping along the SWFZ. Syndepositional movement on unlithified sediments is expressed as sag basins and debris flows in the Mahogany zone. B) In the S2 marker bed, en echelon slump blocks and soft-sediment deformation develops as extension on the fault zone continues above the neutral surface of the continued structural folding. Décollements and small-scale folding occur between the slipping sandstones and the underlying oil shales. C) Late Eocene, after lithification of the sediments, joint sets parallel to the fault zone develops, as does a damage zone. The fault zone experiences relaxation and minor movement on coalesced joint sets, developing a larger damage zone. Slip on all faults decreases downwards, consistent with neutral surface deformation. D) Miocene to present. The development of Basin and Range extension in western Utah creates tension in the Uinta Basin, producing further extension along crustal weak points like the SWFZ. Dip-slip movement occurs on reactivated fault surfaces. Shallow grabens develop across a wider zone of deformation as conjugate fractures move in a normal sense.*

many Laramide faults to be reactivated in a normal sense (figure 23D). The western portion of the SWFZ likely reacted to this extension with continued movement on pre-existing faults and joints. Parts of the fault zone are likely still active with occasional movement as Basin and Range extension continues to pull on the Uinta Basin.

Pleistocene

The SWFZ is well-exposed because of the rapid incision of the Colorado Plateau by the Colorado River and its tributaries due to extension-related base-level drop in the last 6 million years (Pederson and others, 2002; Karlstrom and others, 2008; Aslan and others, 2019).

REFERENCES

Aslan, A., Karlstrom, K.E., Kirby, E., Heizler, M.T., Granger, D.E., Feathers, J.K., Hanson, P.R., and Mahan, S.A., 2019, Resolving time-space histories of Late Cenozoic bedrock incision along the Upper Colorado River, USA: Geomorphology, v. 347, p. 1–26, doi: https://doi.org/10.1016/j.geomorph.2019.106855.

Bader, J.W., 2008, Structural and tectonic evolution of the Cherokee Ridge arch, south-central Wyoming—implications for recurring strike-slip along the Cheyenne belt suture zone: Rocky Mountain Geology, v. 43, no. 1, p. 23–40.

Bader, J.W., 2009, Structural and tectonic evolution of the Douglas Creek arch, the Douglas Creek fault zone, and environs, northwestern Colorado, and northeastern Utah—implications for petroleum accumulation in the Piceance and Uinta Basins: Rocky Mountain Geology, v. 44, no. 2, p. 121–145.

Birgenheier, L.P., and Vanden Berg, M.D., 2011, Core-based integrated sedimentologic, stratigraphic, and geochemical analysis of the oil shale bearing Green River Formation, Uinta Basin, Utah: U.S. Department of Energy, National Energy Technology Laboratory, Topical Report, 19 p.

Boden, T., and Tripp, B.T., 2012, Gilsonite veins of the Uinta Basin, Utah: Utah Geological Survey Special Study 141, 48 p., ISBN 978-155791-856-7.

Bradley, W.H., 1931, Origin and microfossils of the oil shale of the Green River Formation of Colorado and Utah: U.S. Geological Survey Professional Paper 168, 58 p.

Brinkerhoff, R., 2019, Characterizing outcrop growth faults, slump blocks, mud volcanoes and other sedimentary deformation features for use as reservoir analogues for observed features in targeted reservoirs in the Green River Formation, Uinta Basin, Utah [abs.]: American Association of Petroleum Geologists, Rocky Mountain Section Meeting, Search and Discovery Article #51623.

Brinkerhoff, R., and Millard, M., 2019, Using pore system characterization to subdivide the burgeoning Uteland Butte play, Green River Formation, Uinta Basin, Utah [abs.]: American Association of Petroleum Geologists, Rocky Mountain Section Meeting, Search and Discovery Article #11272.

Brinkerhoff, R., and Sprinkel, D.A., 2021, Uinta enigma—the Duchesne fault zone and its impact on the development of the Uinta Basin: Rocky Mountain Association of Geologists, The Outcrop, v. 70, no. 3, p. 16–30.

Cashion, W.B., 1967, Geology and fuel resources of the Green River Formation, southeastern Uinta Basin, Utah and Colorado: U.S. Geological Survey Professional Paper 548, 48 p.

Davis, S.J., Mix, H.T., Weigand, B.A., Carroll, A.R., and Chamberlain, C.P, 2010, Synorogenic evolution of large-scale drainage patterns—isotope paleohydrology of sequential Laramide basins: American Journal of Science, v. 309, p. 549–602.

Dickinson, W.R., Lawton, T.F., and Inman, K.F., 1986, Sandstone detrital modes, central Utah foreland region—stratigraphic record of Cretaceous-Paleogene tectonic evolution: Journal of Sedimentary Petrology, v. 56, no. 2, p. 276–293.

Eckels, M.T., Suek, D.H., Harrison, D.H., and Harrison, P.J., 2004, North Hill Creek 3-D seismic exploration project: Ute Indian Tribe, Uintah & Ouray Reservation, Uintah County: U.S Department of Energy, Final Technical Report, 26 p.

Ford, G.L., Pyles, D.R., and Dechesne, M., 2016, Stratigraphic architecture of a fluvial-lacustrine basin-fill succession at Desolation Canyon, Uinta Basin, Utah—reference to Walthers' Law and implications for the petroleum industry: The Mountain Geologist, v. 53, no. 1, p. 5–28.

Fouch, T.D., 1976, Revision of the lower part of the Tertiary system in the central and western Uinta Basin, Utah: U.S. Geological Survey Bulletin 1405-C, p. C1–C7.

Fouch, T.D., Cashion, W.B., Ryder, R.T., and Campbell, J.A., 1976, Field guide to lacustrine and related nonmarine depositional environments in Tertiary rocks, Uinta Basin, Utah, in Epis, R.C., and Weimer, R.J., editors, Professional contributions of Colorado School of Mines-studies in Colorado field geology, Number 8: Colorado School of Mines, p. 358–385.

Fouch, T.D., Nuccio, V.F., Anders, D.E., Rice, D.D., Pitman, J.K., and Mast, R.F., 1994a, Green River (!) petroleum system, Uinta Basin, Utah, U.S.A., *in* Magoon, L.B., and Dow, W.G., editors, The petroleum system—from source to trap: American Association of Petroleum Geologists Memoir 60, p. 399–421.

Fouch, T.D., Wandrey, C.J., Taylor, D.J., Butler, C.B., Miller, J.J., Prensky, S.E., Boone, L.E., Schmoker, J.W., Crovelli, R.A., Beeman, 1994b, Oil and Gas Resources of U.S. Naval Oil Shale Reserves 1 and 3, Colorado, and Reserve 2, Utah: Open-File Report 94-427, U.S. Department of Energy Contract No. DE-AT21-93-MC30141, https://doi.org/10.3133/ofr94427.

Grabowski, G.J., Jr., and Peaver, D.R., 1985, Sedimentology and petrology of profundal lacustrine sediments, Mahogany zone of the Green River Formation, Piceance Creek Basin, northwest Colorado, *in* Crevello, P.D., and Harris, P.M., editors, Deep-water carbonates—buildups, turbidites, debris flows and chalk: Society for Sedimentary Geology (SEPM) Core Workshop 6, p. 386–430.

Grout, M.A., and Verbeek, E.R., 1998, Tectonic and paleostress significance of the regional joint network of the central Paradox Basin, Utah and Colorado: U.S. Geological Survey Bulletin 2158, p. 151–166.

Howe, J., and Klinger, R., 2021, Evidence for Quaternary activity on the Duchesne-Pleasant Valley fault, Uinta Basin, Utah: Seismological Society of America Seismological Research Letters, v. 92, no. 2B, p. 1335, doi: https://doi.org/10.1785-/0220210025.

Johnson, R.C., 1985, Early Cenozoic history of the

Uinta and Piceance Creek Basins, Utah and Colorado, with special reference to the development of Eocene Lake Uinta, *in* Flores R.M., and Kaplan, S.S., editors, Cenozoic paleogeography of the west-central United States: Society for Sedimentary Geology (SEPM), Rocky Mountain Section, Rocky Mountain Paleogeography Symposium 3, p. 247–276, online, http://archives.datapages.com/data/rocky_sepm/data/023/023001/247_rocky_mount230247.htm.

Johnson, R.C., and Finn, T.M., 1986, Cretaceous through Holocene history of the Douglas Creek arch, Colorado and Utah, *in* Stone, D.S., editor, New interpretations of northwest Colorado geology: Rocky Mountain Association of Geologists Guidebook, p. 77–95.

Karlstrom, K.E., Crow, R., Crossey, L.J., Coblentz, D., and Van Wijk, J.W., 2008, Model for tectonically driven incision of the younger than 6 Ma Grand Canyon: Geology, v. 36, no. 11, p. 835, doi: 10.1130/g25032a.1.

Keighley, D., 2013, Outcrop chemostratigraphic correlation of the upper Green River Formation in the Uinta Basin, Utah—Mahogany oil shale zone to the Uinta Formation: Utah Geological Survey Miscellaneous Publication 13-1, p. 30.

Keighley, D., Töro, B., Vanden Berg, M.D., and Pratt, B.R., 2015, Deformation within the Mahogany oil shale zone of the Green River Formation at Sand Wash, eastern Utah, USA, *in* Vanden Berg, M.D., Ressetar, R., and Birgenheier, L.P., editors, Geology of Utah's Uinta Basin and Uinta Mountains: Utah Geological Association Publication 44, p. 423–438.

Marshak, S., Nelson, W.J., and McBride, J.H., 2003, Phanerzoic strike-slip faulting in the continental interior platform of the United States: examples from the Laramide Orogen, Midcontinent, and Ancestral Rocky Mountains, *from*: Storti, F., Holdsworth, R.E. and Salvani, F. (eds) *Intraplate Strike-Slip Deformation Belts.* Geological Society, London, Special Publications, 210, 159-184, 0305 -8719/03/$15.

Mederos, S., Tikoff, B., and Bankey, V., 2005, Geometry, timing, and continuity of the Rock Springs uplift, Wyoming, and Douglas Creek arch, Colorado—implications for uplift mechanisms in the Rocky Mountain foreland, U.S.A.: Rocky Mountain Geology, v. 40, p. 167–191.

Mews, K., Mustafa, A.M., and Barati, Rh., 2019, A review of brittleness index correlations for unconventional tight and ultra-tight reservoirs: Geosciences, v. 9, 10.3390/geosciences9070319.

Morgan, C.D., 2003, Geologic guide and road logs of the Willow Creek, Indian, Soldier Creek, Nine Mile, Gate, and Desolation Canyons, Uinta Basin, Utah: Utah Geological Survey Open-File Report 407, 74 p., https://geology.utah.gov/resources/energy/oil-gas/green-river-formation-project/.

Morgan, C.D., McClure, K.P., Bereskin, S.R., and McPherson, M., 2002, A preliminary discussion of fault styles in the southwest Uinta Basin, Utah [abs.]: American Association of Petroleum Geologists, Rocky Mountain Section Meeting Program with Abstracts, https://geology.utah.gov/resources/energy/oil-gas/green-river-formation-project/.

Osmond, J.C., 1965, Geologic history of the Uinta basin, Utah: American Association of Petroleum Geologists Bulletin, v. 49, n. 11, p. 1957-1973.

Pederson, J., Karlstrom, K., Sharp, W., and McIntosh, W., 2002, Differential incision of the Grand Canyon related to Quaternary faulting—constraints from U-series and Ar/Ar dating: Geology, v. 30, no. 8, p. 739–742.

Remy, R., 1992, Stratigraphy of the Eocene part of the Green River Formation in the south- central part of the Uinta Basin, Utah: U.S. Geological Survey Bulletin B 1787-BB, p. BB1–BB69.

Smith, M.E., Carroll, A.R., and Singer, B.S., 2008, Synoptic reconstruction of a major ancient lake system—Eocene Green River Formation, western United States: Geological Society of America Bulletin, v. 120, no. 1/2, p. 54–84, doi: 10.1130/B26073.1.

Sprinkel, D.A., 2009, Interim Geologic Map of the Seep Ridge 30' x 60' quadrangle: Utah Geological Survey, Utah Geological Survey Open-File Report 549DM, 3 plates.

Sprinkel, D.A., 2014, The Uinta Mountains—a tale of two geographies and more: Utah Geological Survey, Survey Notes, v. 46, no. 3, p. 1–4.

Sprinkel, D.A., 2018, Mysteries of the Uinta Mountains—commonly asked questions and answers: Utah Geological Survey, Survey Notes, v. 50, no. 3, p. 1–3.

Stone, D.S., 1977, Tectonic history of the Uncompahgre uplift, *in* Veal, H.K. editor, Rocky exploration frontiers of the central and southern Rockies: Rocky Mountain Association of Geologists Guidebook, p. 23–30.

Töro, B., and Pratt, B.R., 2015, Characteristics and implications of sedimentary deformation features in the Green River Formation (Eocene) in Utah and Colorado, *in* Vanden Berg, M.D., Ressetar, R., and Birgenheier, L.P., editors, Geology of Utah's Uinta Basin and Uinta Mountains: Utah Geological Association Publication 44, p. 371–422.

Verbeek, E.R., and Grout, M.A., 1993, Geometry and

structural evolution of gilsonite dikes in the eastern Uinta Basin, Utah: U.S. Geological Survey Bulletin 1787-HH, 42 p., 1 plate.

Wawrzyniec, T.F., Geissman, J.W., Melker, M.D., and Hubbard, M., 2002, Dextral shear along the eastern margin of the Colorado Plateau—a kinematic link between Laramide contraction and Rio Grande rifting (Ca. 75–13 Ma): Journal of Geology, v. 110, p. 305–324.